Natural Resources Research (© 2023)
https://doi.org/10.1007/s11053-023-10180-w

Original Paper

3D Static Modeling and CO_2 Static Storage Estimation of the Hydrocarbon-Depleted Charis Reservoir, Bredasdorp Basin, South Africa

Blessing Ayotomiwa Afolayan,[1,3] Eric Mackay,[2] and Mimonitu Opuwari[1]

Received 7 November 2022; accepted 4 March 2023

An essential greenhouse gas effect mitigation technology is carbon capture, utilization and storage, with carbon dioxide (CO_2) injection into underground geological formations as a core of carbon sequestration. Developing a robust 3D static model of the formation of interest for CO_2 storage is paramount to deduce its facies changes and petrophysical properties. This study investigates a depleted oilfield reservoir within the Bredasdorp Basin, offshore South Africa. It is a sandstone reservoir with effective porosity mean of 13.92% and dominant permeability values of 100–560 mD (1 mD = 9.869233×10^{-16} m^2). The petrophysical properties are facies controlled, as the southwestern area with siltstone and shale facies has reduced porosity and permeability. The volume of shale model shows that the reservoir is composed of clean sands, and water saturation is 10–90%, hence suitable for CO_2 storage based on petrophysical characteristics. Static storage capacity of the reservoir as virgin aquifer and virgin oilfield estimates sequestration of 0.71 Mt (million tons) and 1.62 Mt of CO_2, respectively. Sensitivity studies showed reservoir depletion at bubble point pressure increased storage capacity more than twice the depletion at initial reservoir pressure. Reservoir pressure below bubble point with the presence of gas cap also increased storage capacity markedly.

KEY WORDS: 3D static model, Facies, Petrophysical properties, Static storage capacity, Sensitivity studies, Bredasdorp basin.

INTRODUCTION

Climate researchers and governments worldwide are not in denial of the reality of climate change, and the main culprit is man's continual dependence on fossil fuels, with the 2015 Paris Agreement setting the world on course to drastically cut down emissions of anthropogenic carbon dioxide (CO_2) and reducing global warmth increment under 1.5 °C (UNFCCC, 2015; IPCC, 2018). As the International Energy Agency (IEA) estimated, the energy demand could escalate by well-nigh 4% by 2030, with the demand mainly satisfied by fossil fuels (Yelebe & Samuel, 2015).

Around 90% of South Africa's vital energy is satisfied by petroleum derivatives, and coal delivers 92% of power generation countrywide (South Africa Department of Energy, 2009). South Africa has vast coal reservoirs used predominantly in power generation, production of liquid fuels and a direct supply of heat and steam in various industrial processes.

[1]Petroleum Geosciences Research Group, Department of Earth Sciences, University of the Western Cape, Bellville 7535, Republic of South Africa.
[2]Institute of Petroleum Engineering, Heriot-Watt University, Riccarton, Edinburgh EH14 4AS, UK.
[3]To whom correspondence should be addressed; e-mail: 3993275@myuwc.ac.za

Presently, emissions of CO_2 are thought to exceed 400 Mt (million tons) per year in South Africa (Cloete, 2010). One of the specialized methodologies that can be utilized to moderate worldwide environmental change in non-renewable energy-centered nations such as South Africa is carbon capture, utilization and storage (CCUS) (Anastassia et al., 2010; Viljoen et al., 2010; Chabangu et al., 2014a, 2014b; Tsuji et al., 2014; Kempka et al., 2017; Bandilla et al., 2019; Yan & Zhang, 2019; Alcalde et al., 2021).

Storage of CO_2 in deep geological formations involves capturing and separating from an industrial source, onward conveyance and injection into underground geologic reservoirs for permanent storage. Finally, it is measured, monitored and verified that it stays in the storage formation (Würdemann et al., 2010). From Meer (1995), Kumar et al. (2005), Teletzke & Lu (2013), Ojo & Tse (2016), Bui et al. (2018) and Alcalde et al. (2021), the typical geological indicators for the perfect spot for CO_2 storage involve:

- A reservoir rock or unit (such as hydrocarbon-depleted reservoirs, deep saline aquifers, coal seams, and salt caverns), with sufficient porosity and permeability, allowing injection and persistent storage of CO_2.
- The reservoir units occur at depths exceeding 800 m from mean sea level, ensuring reservoir pressure and temperature conditions (typically 73.7 bar and 31 °C geometric and geothermal gradient) allow CO_2 existence in a dense supercritical form.
- An impermeable rock acts as a seal above the reservoir, preventing upward migration of CO_2.

The injection and geological storing of CO_2 have been utilized for a considerable time to enhance optimization in oil and gas fields, while storage of gas and other substances in geological reservoirs has likewise been ongoing for decades (Viljoen et al., 2010; Vincent et al., 2013). Equivalent geological factors keeping commercial quantities of hydrocarbon in the subsurface for geologic time are currently being applied for CO_2 storage. Depleted petroleum fields can geologically host CO_2 because their hydrocarbon retention ability has been demonstrated, as they have held barrels of hydrocarbon for geologic time, with accompanying massive geological and engineering data gathered from the fields for detailed reservoir characterization or while in production to improve oil and gas recovery (Alcalde et al., 2019, 2021; Ghanbari et al., 2020).

The drive to attain accurate resource estimation, efficient production, and improve cost effectiveness and economic viability of subsurface resources has necessitated the modeling of rock properties and fluid characteristics in a 3D space, using seismic, core and well logs data (Khadragy et al., 2017; Ali et al., 2021; Ayodele et al., 2021; Othman et al., 2021; Opuwari et al., 2022). Therefore, an integral aspect of site appraisal before CO_2 injection is a methodic retention assessment, i.e., construction of a robust 3D static model of these geologic formations found at great depths (Smith et al., 2012; Ojo & Tse, 2016; Shariatipour et al., 2016; Ampomah et al., 2017; Niri, 2018; Abdullah et al., 2021), because it enables modeling of multiplex reservoirs having lateral and vertical lithologic variations, with an improved knowledge of reservoir properties distribution leading to enhanced volumetric estimation, risk and uncertainty analysis, predictions of fluid flow and field development plans (Abdel-Fattah et al., 2018; Adelu et al., 2019; Rahimi & Riahi, 2020; Radwan et al. 2022a, 2022b; Sarhan et al., 2022).

With CO_2 emissions of approximately 430 Mt (million tons) annually (Boden et al., 2011), the South African government has acceded to the global demand for reduction in greenhouse gas emissions via some international accords (Winkler et al., 2002; Hietkamp et al., 2004). The country has further investigated the potentials of CO_2 storage in South Africa, identified possible sites (saline aquifers, hydrocarbon-depleted reservoirs, coal seams and basement rocks) and estimated their storage capacities, the study revealed geological formations in South Africa can store an estimated 150 Gt (giga tons) of CO_2, but onshore sites in the Zululand and Algoa basins can only hold below 2% of this (Cloete, 2010; Chabangu et al., 2014a, 2014b; Tibane et al., 2021). This has necessitated the drive to assess the potentials of offshore lying basins (Outeniqua and Orange basins) for CO_2 storage, with the hydrocarbon-depleted reservoirs of greater interest due to availability of data such as wireline logs, seismic, engineering and production data for adequate reservoir assessment and de-risking.

The E-BD field is a depleted oilfield within the offshore lying Bredasdorp Basin, a sub-basin of the Outeniqua basin, southern South Africa. Wildcat,

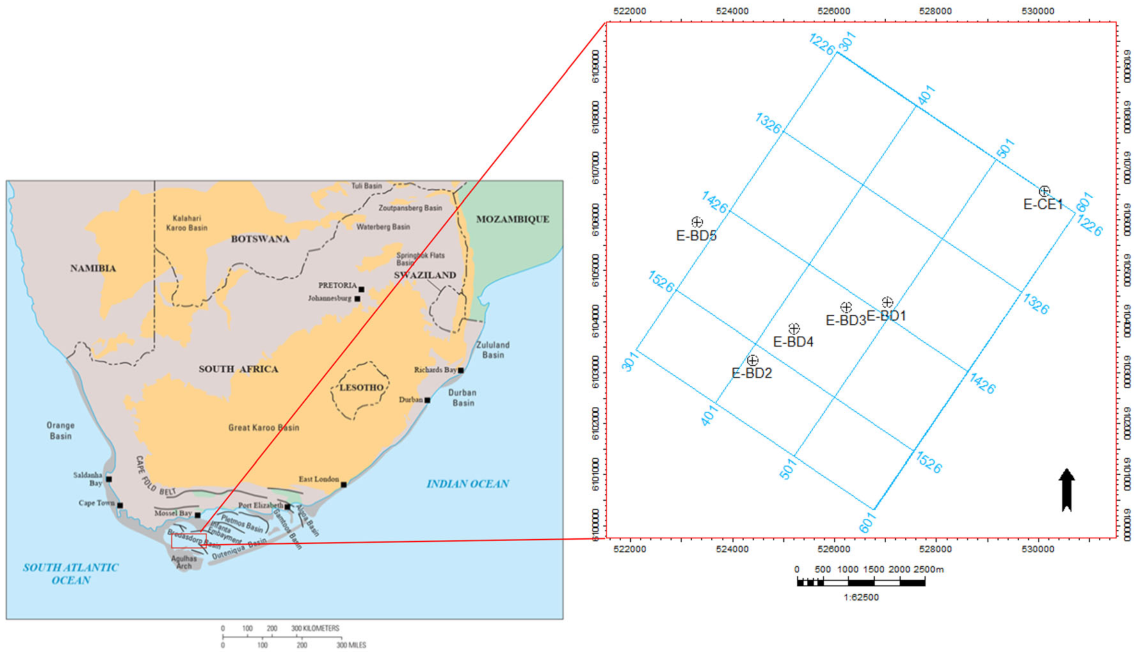

Figure 1. The study area map, with wells and seismic cube offshore South Africa, produced from Petrel 2018.2 software (https://usoftly.com/product/schlumberger-petrel-2018-2-7/) modified (Petroleum Agency of South Africa, 2017).

appraisal, development, and production wells have been drilled for oil extraction in the field, leading to its final abandonment. From available data, there exists no public/published work on a 3D static model of an oilfield in the Bredasdorp Basin. This study presents a detailed production of a 3D geological model, integrating 3D seismic data, well logs and available geological information for a good grasp of the geometric dispersal of continuous petrophysical properties such as effective porosity, water saturation, permeability, and discrete properties such as facies distribution in the oilfield. This model also serves as the primary input for dynamic simulation of the oilfield as a potential CO_2 sink.

Geological Setting

The Bredasdorp basin is a prolific hydrocarbon province off the South African coast, and lying beneath the Indian Ocean (Parker, 2014; Acho, 2015; Magoba & Opuwari, 2017; Opuwari et al., 2022). It is 200 km long and 80 km wide, covering approximately 18,000 km^2, hosting most of South Africa's prospects and discoveries. The study area (Fig. 1), located within the Bredasdorp Basin, a sub-basin and part of a series of en echelon sub-basins within the Outeniqua Basin, is a synrift half-graben passive margin basin bounded by the Infanta arch and Agulhas arch in the north and south, respectively, the arches being basement highs composed of the Cape Supergroup sediments, metamorphic rocks, and granites dated to the Precambrian (Davies, 1997; Nfor, 2011; Opuwari et al., 2022), overlain with varying thicknesses of drift sediments.

The sedimentary successions and tectonic history of the Bredasdorp basin have been well documented, with the distribution of sediments largely eustasy-dependent (Viljoen et al., 2010; Opuwari et al., 2022) (Fig. 2). The Bredasdorp basin was infilled by sediments derived from the denudation of the shallow, deep and transitional marine environments of the Cape and Karoo Supergroups (Mcmillan et al., 1997). The Cape fold belt, extending both offshore and onshore on South Africa's coast, resulted from the Cape Supergroup folding during the Cape orogeny (Haelbich et al., 1983). Towering on the top of a retro arc foreland basin is the succession of the Karoo Supergroup of alluvial, marine, deltaic and glacial origins deposited from late Carboniferous to early Jurassic at the onset of erosion and subduction (Dingle, 1983; Smith,

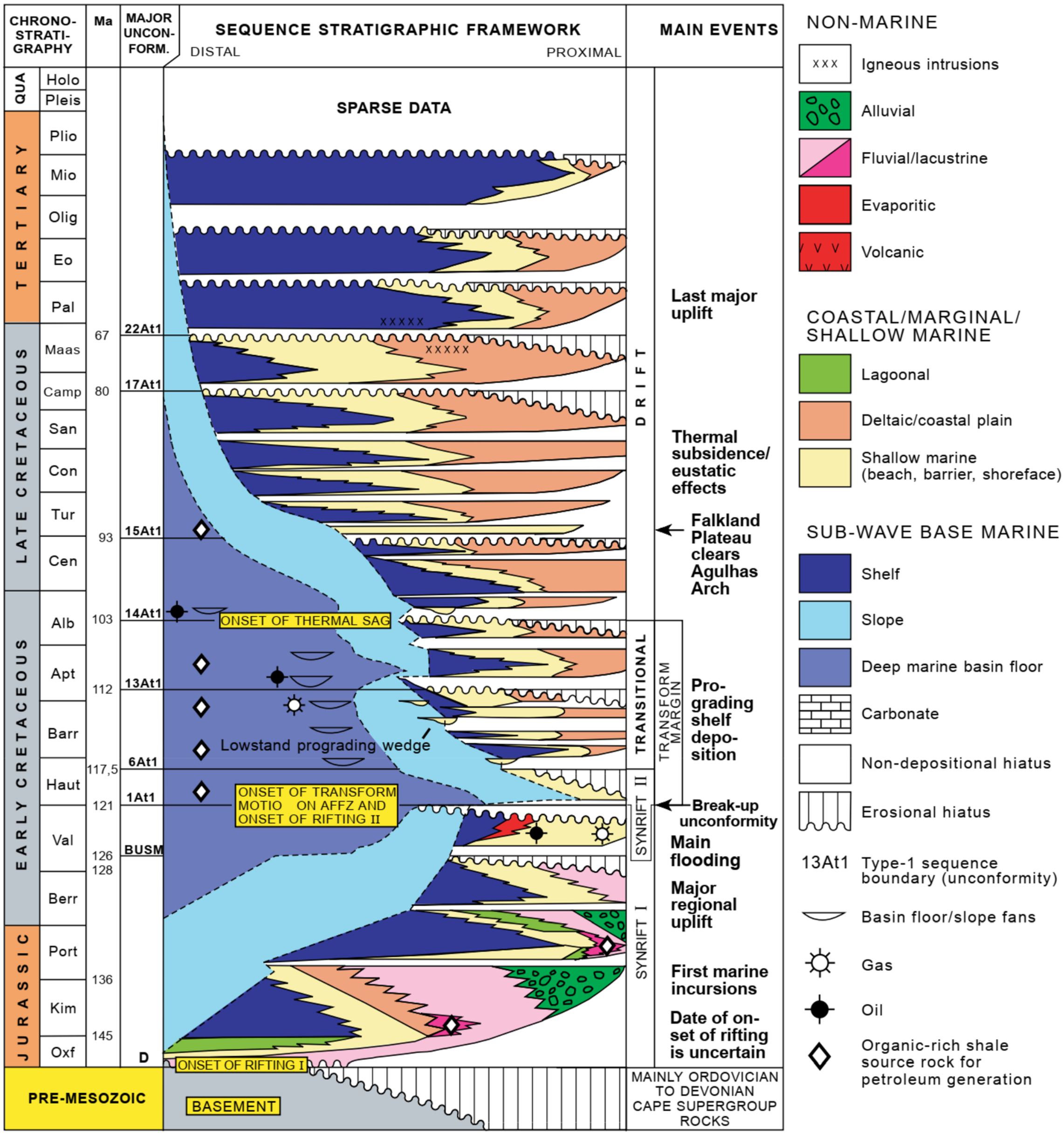

Figure 2. Generalized chronostratigraphic map of the Bredasdorp Basin (modified after Brown et al., 1995; Petroleum Agency of South Africa, 2017).

1990; Brown et al., 1995; Jungslager, 1999; Broad et al., 2012). At the cessation of the Karoo Supergroup erosion, the Eastern Gondwana showed records of rifting, and the synrift half grabens of the Bredasdorp basin appeared (Mcmillan et al., 1997; Hendricks, 2019). Although the main source rock of the oil in the basin is the deep marine mature shales deposited in the mid-Aptian (Fig. 2), the synrift shelf and drift section deep marine turbidite sandstones form the two major basinal reservoirs, while the drift shales of marine origin act as the primary seals. Stratigraphic traps in the drift section and structural traps as tilted fault blocks, in the synrift, are well represented in the Bredasdorp basin (Jungslager, 1999; Petroleum Agency of South Africa, 2017).

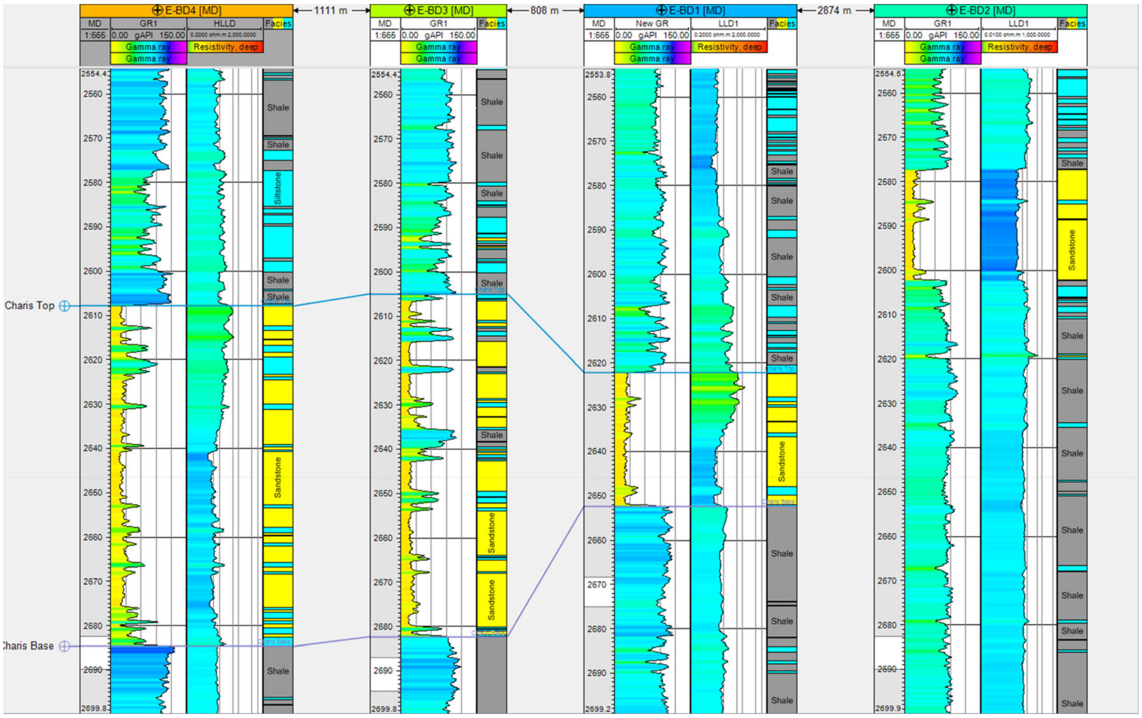

Figure 3. Stratigraphic correlation of log responses through the hydrocarbon column in the drilled wells in the oilfield.

METHODOLOGY

Materials

Data used for the study were made available by the Petroleum Agency South Africa (PTY) Limited (PASA). The work integrated 3D seismic volume (SEG-Y format), formation tops, check shot data, wireline logs, geological reports from the oilfield and core data. Six wells were made available, namely E-BD1, E-BD2, E-BD3, E-BD4, E-BD5 and E-CE1. Wells E-BD5 and E-CE1 were outside the seismic cube (Fig. 1).

Identification of Charis Reservoir and Hydrocarbon Bearing Zone

Gamma-ray (GR) and deep resistivity logs were used to identify potential hydrocarbon-bearing sands/reservoirs. Using gamma-ray, the identification of facies and lithology correlation from well log between the studied wells. For example, $\leq$ 40 API represented sandstone, 40–95 API was siltstone, with shale indicated by an API $\geq$ 95. Hence, the three facies identified were shale, siltstone and sandstone (Fig. 3). This process gave the facies distribution in the model generated for the reservoir and enabled facies correlation between wells. Resistivity log aided the identification of possible oil–water contact (OWC), i.e., a differentiation between oil and water-bearing zones (Saadu & Nwankwo, 2018; Adelu et al., 2019; Ayodele et al., 2021).

The reservoir (named Charis) (Fig. 3) was intersected in well E-BD1 from 2622 to 2653 m (31 m), 2605–2682 m (77 m) in well E-BD3 and 2607–2684 m (77 m) in well E-BD4, with the OWC at 2639 m in E-BD1 and 2640 m in E-BD4. (There was no deep resistivity log for E-BD3.) The E-BD2 well was drilled to test commercial quantities of oil stored in the sandstones intersected in the E-BD1 well, but lying above the OWC in E-BD1 and E-BD4 was a 25 m (2577–2602 m) water-saturated sandstone, suggesting the reservoir rocks encountered in E-BD1 did not continue into E-BD2 (Fig. 3). The E-BD2 well was therefore excluded from the correlation and further analysis because the Charis reservoir did not extend into this well. The Charis reservoir intersected in E-BD1, E-BD3 and

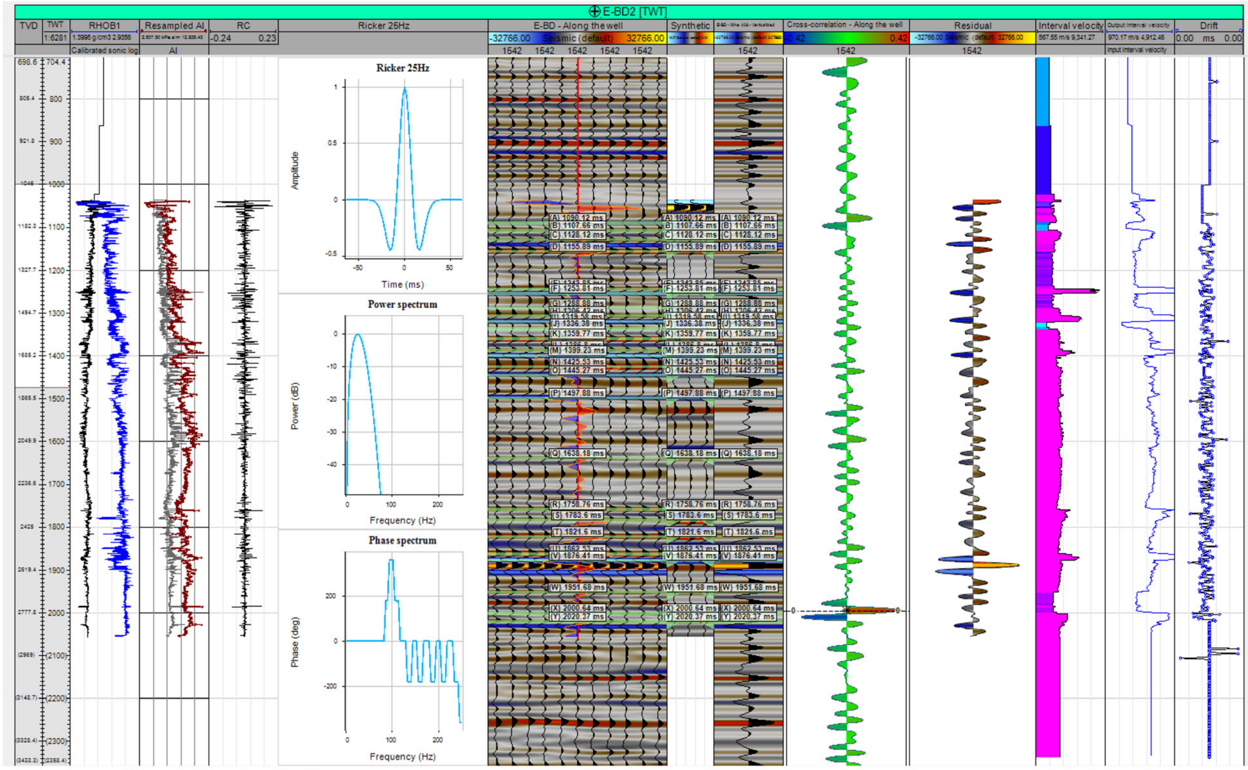

Figure 4. Well-to-seismic tie from E-BD2.

E-BD4 was then subjected to further seismic and petrophysical investigations for modeling.

Seismic Interpretation

This started with tying seismic (in the time domain) to well data (measured in depth) (called the seismic-to-well tie) using the Petrel 2018.2 software developed by Schlumberger (Fig. 4). The tie was done by using the provided check shot survey from well EBD-1, and reflection coefficients (RC) and acoustic impedance (AI) were generated using density (RHOB1) and calibrated sonic log (Fig. 4). The well-to-seismic tie is principally jeered toward correlating the top and base of the hydrocarbon-bearing sand with their specific reflections on seismic. Seismic horizons (top and base of sands) were already identified on well logs, and structural discontinuities (fault) mapping over the entire grid of the seismic cube was done immediately after the well-to-seismic tie (Fig. 5). The horizons and faults were mapped in time guardedly (though there were only minor faults with no major impact on the reservoir within the entire grid). Subsequently, time was converted to depth with the 3D velocity model developed by integrating the well velocity data and the seismic horizons. The depth conversion supplied the horizons and faults in depth grids, serving as input for the 3D static model, and enabled the generation of structure maps and an isopach (thickness) map (Figs. 5, 6, 7) (Khadragy et al., 2017; Ali et al., 2021; Ayodele et al., 2021; Okoli et al., 2021; Othman et al., 2021; Sarhan et al., 2022).

Petrophysical Evaluation

Wireline logs (such as resistivity, neutron, density, gamma-ray, and sonic) were subjected to petrophysical examination using Interactive Petrophysics (IP) software (version 2021) to calculate properties of the reservoir such as volume of shale, net-to-gross (NTG), effective porosity (φ_{eff}), permeability, water saturation (S_w), and reservoir thickness. The following linear formula was used to

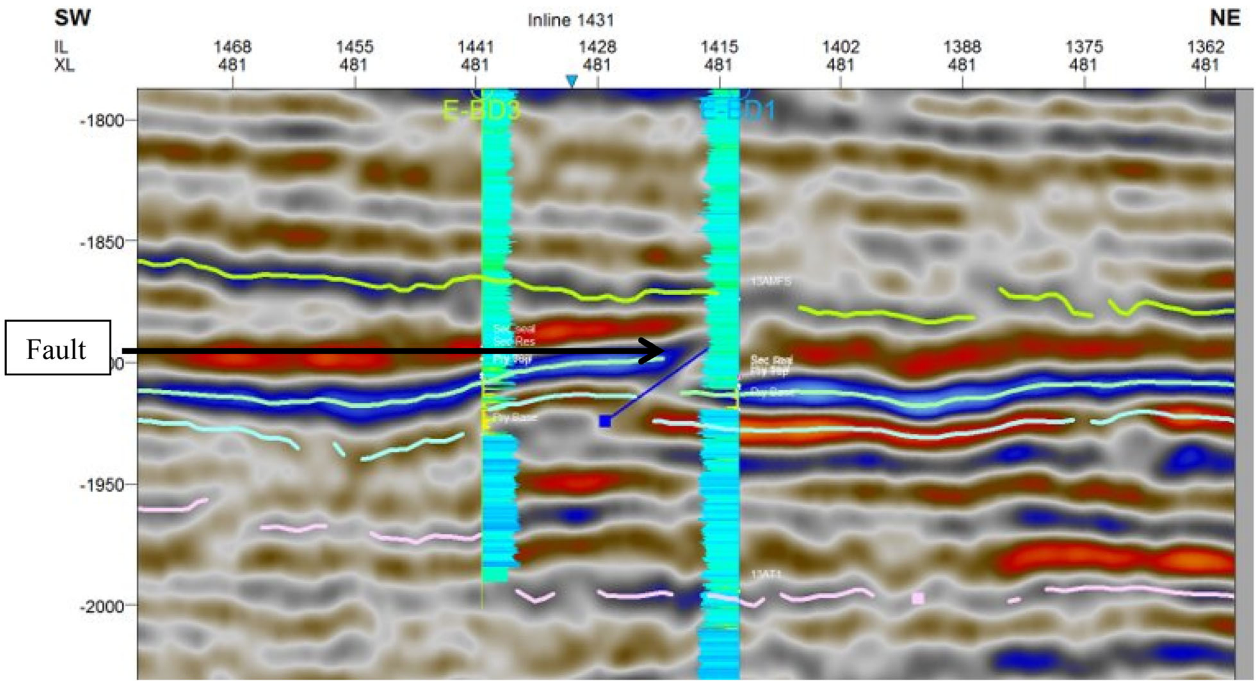

Figure 5. Seismic section showing a mapped fault and some horizons.

obtain the gamma-ray index (IGR) from the log (Asquith & Gibson, 1982), thus:

$$\mathrm{IGR} = \frac{Gr\ \log - Gr\ minimum}{Gr\ maximum - Gr\ minimum} \quad (1)$$

$$Vsh = 0.33(2^{(2*\mathrm{IGR})} - 1 \quad (2)$$

where *Gr* log is target formation gamma-ray log reading, *Gr minimum* is minimum gamma-ray log reading; and *Gr maximum* is maximum gamma-ray log reading. Corrections were then performed to Eq. 1 using the nonlinear Larionov method (Larionov, 1969). The IGR value gotten from Eq. 1 was then used in the volume of shale estimation by Eq. 2.

Density log-derived total porosity [ϕt (%)] was estimated as:

$$\phi t = \frac{\rho ma - \rho b}{\rho ma - \rho fl} \quad (3)$$

where ρma is density (g/cm^3) of matrix; ρb is density (g/cm^3) log reading, and ρfl is density (g/cm^3) of fluid. An average matrix density of 2.67 g/cm^3 from core grain density was used (Asquith & Gibson, 1982; Ayodele et al., 2021). By applying a shale correction to the calculated ϕt, effective porosity was obtained as:

$$\text{Effective porosity} = \phi t - Vsh \quad (4)$$

An empirical equation from the core porosity versus core permeability cross-plot was derived to estimate permeability using the hydraulic flow unit concept. The input parameters were core porosity and core permeability data. This method has been used extensively and successfully by many researchers (e.g., Amaefule et al., 1993; Abbaszadeh et al., 1996; Perez et al., 2003; Kadkhodaie-Ilkhchi et al., 2013; Nabawy & Al-Azazi, 2015; Opuwari et al., 2021, 2022; Radwan et al., 2021).

Water saturation was estimated as (Archie, 1942):

$$Sw = \left(\frac{aRw}{\phi^m Rt}\right)^{1/n} \quad (5)$$

where *a* is coefficient of formation factor, *Rw* is water resistivity (ohm), *m* is cementation exponent, *Rt* is true resistivity (ohm) of the formation, *n* is saturation exponent, and ϕ is porosity (dec). Estimated results from the log were calibrated with core measurements as supplied by the Petroleum Agency

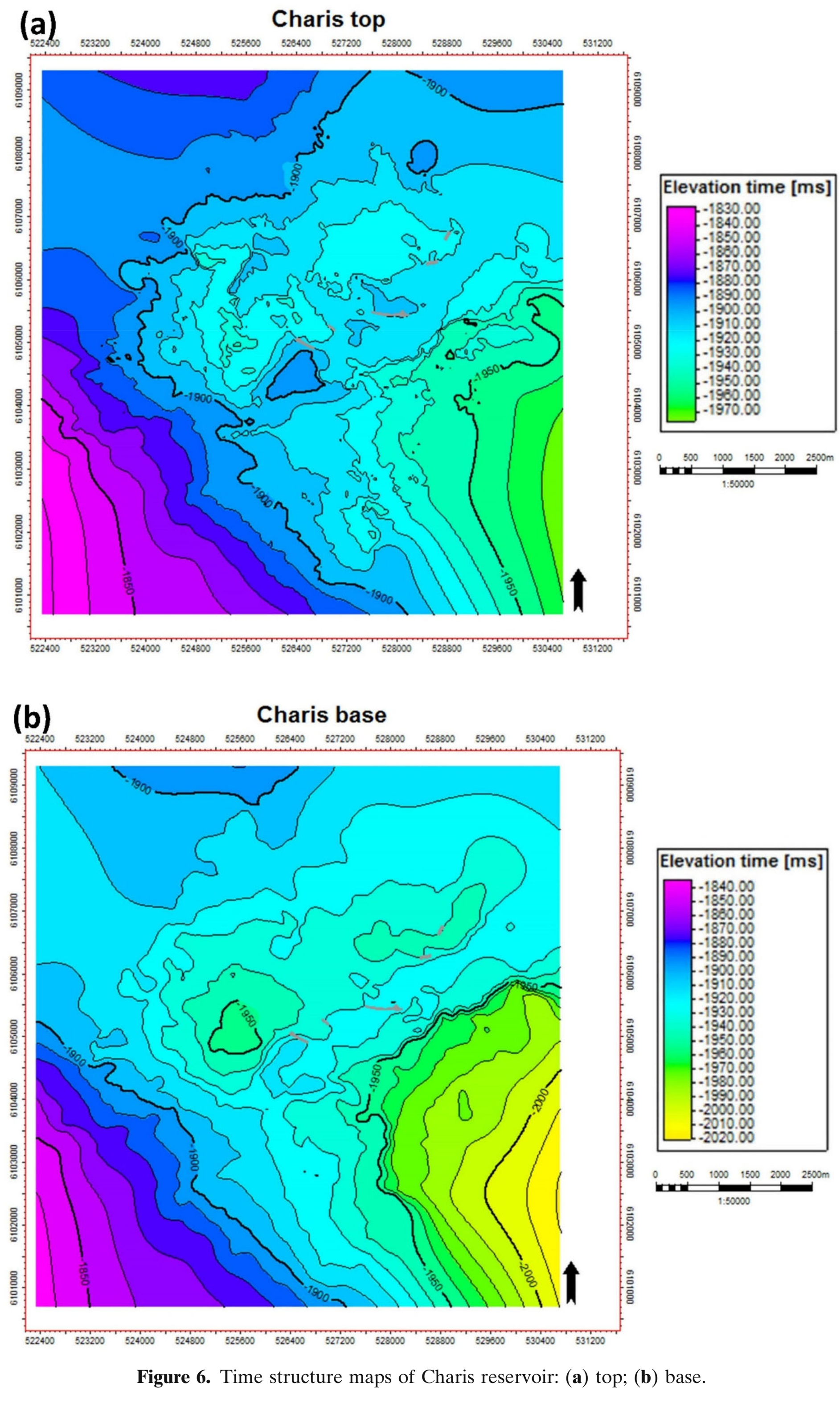

Figure 6. Time structure maps of Charis reservoir: (**a**) top; (**b**) base.

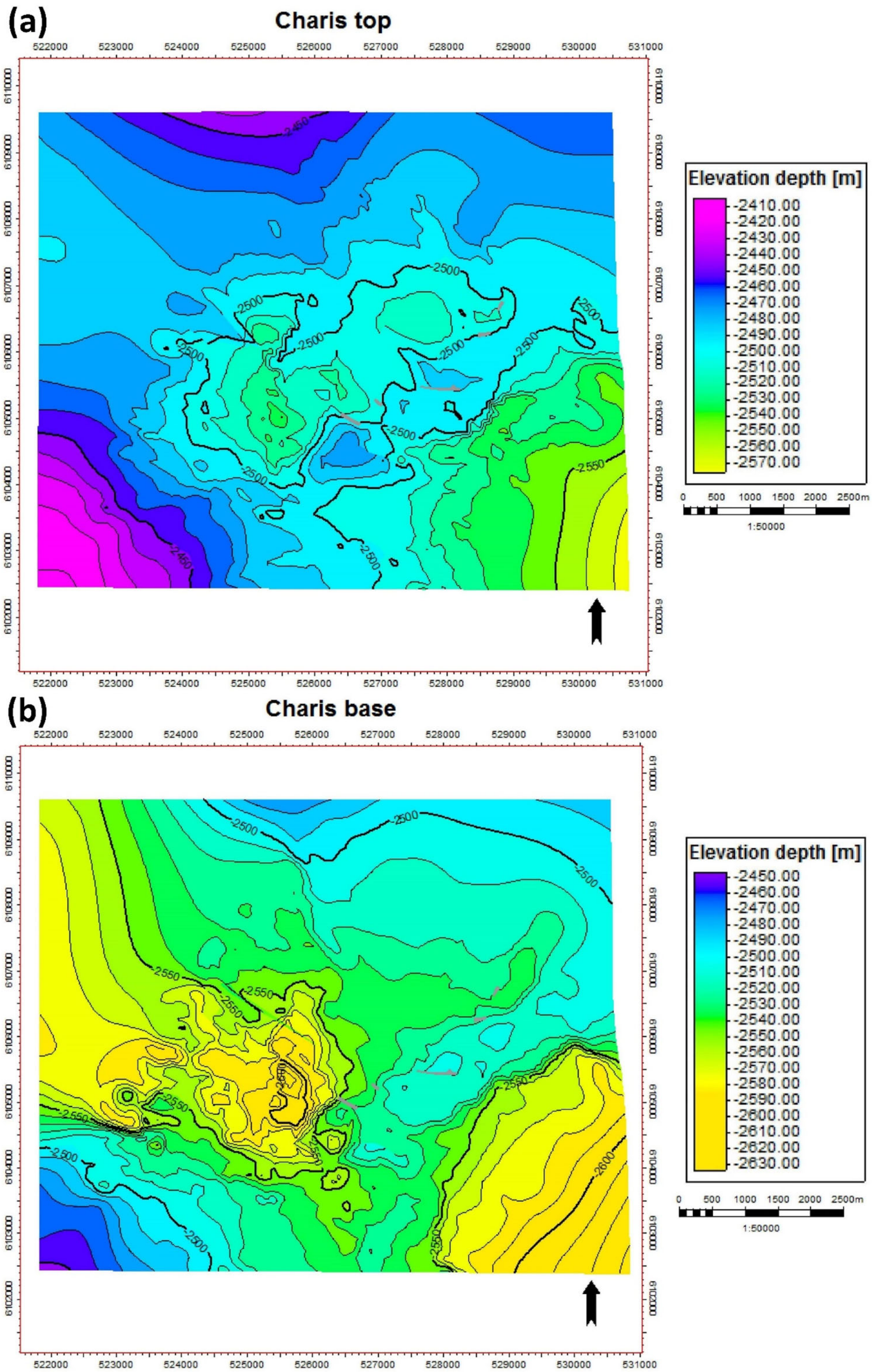

Figure 7. Depth structure maps of Charis reservoir: (**a**) top; (**b**) base.

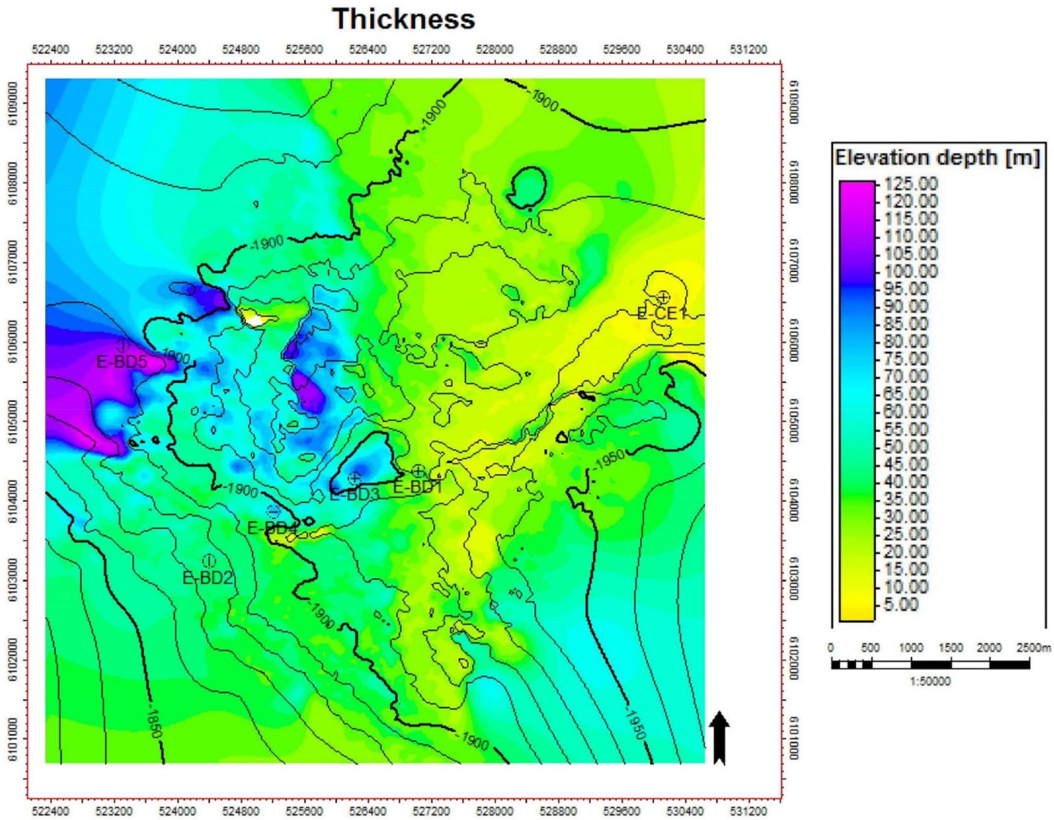

Figure 8. Isopach map of the Charis reservoir.

South Africa (PTY) Limited (PASA), which gave a good level of reliability to the results (Figs. 9, 10).

RESULT AND DISCUSSION

Time and Depth Map of the Charis Reservoir

The time contour map of the Charis reservoir shows a time increase in the eastern and southeastern areas, with maximum values of about 1.97 and 1.95 s, respectively, indicative of low structural features (Ali et al., 2021). There was a decrease in the TWTs (two-way travel times) in the northern and western parts with values around 1.9 and 1.88 s, with the southwestern area recording the most negligible value of about 1.83 s, indicative of high structural features (Fig. 6a, b). The basal map of the Charis reservoir records similar characteristics, with the time increase in the eastern and southeastern areas, with values around 0.2 s, a decrease of TWTs in the northern and western parts with values around 1.9 and 1.89 s, and the most negligible value of about 1.84 s in the southwestern portion of the map. The depth maps (Fig. 7a, b) of the Charis reservoir show a general southeast, central to northwest deepening with peak values reaching − 2630 m and shallowing to the southwest and northern areas, having values of − 2450 m and − 2480 m, respectively.

Isopach Map of the Charis Reservoir

The Charis reservoir's isopach map was generated by subtracting the Charis reservoir base depth map from the top depth map (refer to Fig. 3 for stratigraphic positions). As a result, the generated isopach map (Fig. 8) reflected that the Charis

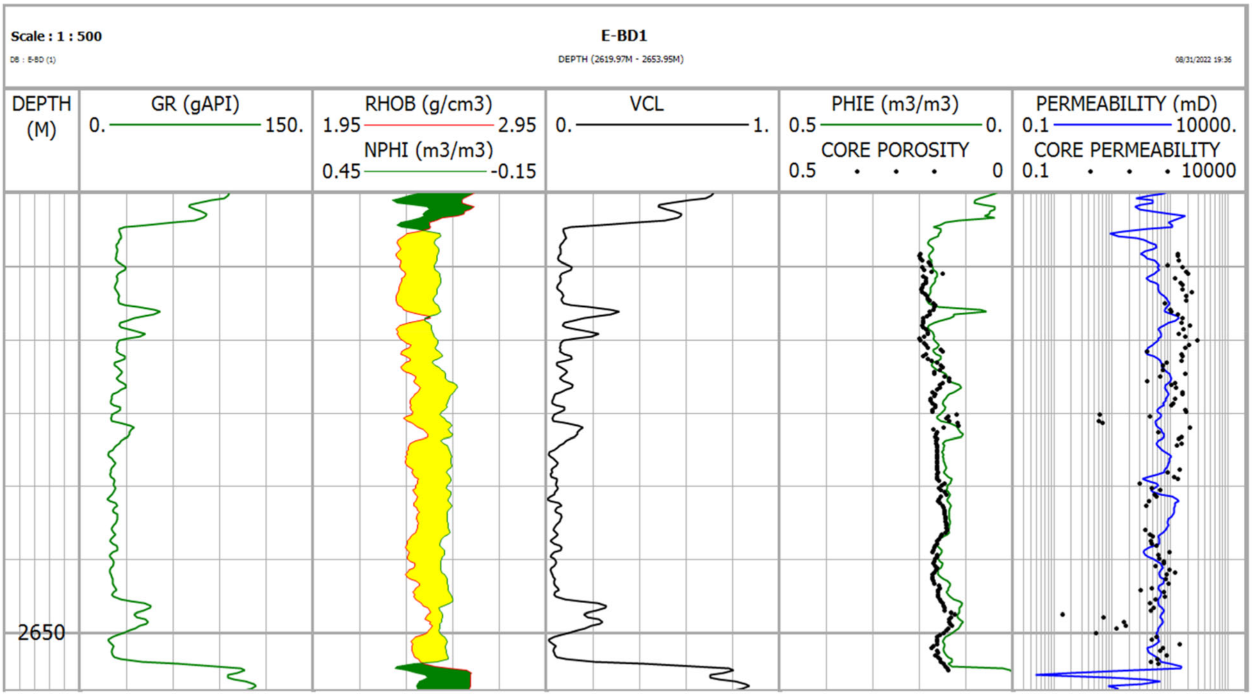

Figure 9. Charis reservoir litho-saturation cross-plots from well E-BD1.

reservoir thickness increased markedly in the northwest and central sections of the reservoir, with the basinal area having sediment thickness of around 125 m in the northwest and down to between 95 and 100 m in the central portion of the reservoir. However, thickness decreased in the northeastern region to as low as 5 m.

Lithology and Petrophysical Characteristics of the Charis reservoir

The stratigraphy of the Charis reservoir, as deduced from core data and well logging analyses, is composed of three facies; shales, predominantly clean good, quality channel sandstones (coarse to fine-grained); and thin siltstone interbeds. Petrophysical data logs of some selected wells and a summary of the petrophysical properties of the Charis reservoir are presented in Figures 9 and 10 and Table 1.

3D Facies Model

Facies log upscaling in the available wells is the first stage of building a 3D facies model of a reservoir (Ali et al., 2020a, 2020b, 2021; Othman et al., 2021; Radwan et al., 2022a, 2022b), with the assigned facies values in the log from the penetrated wells vertically and horizontally distributed to fill the whole 3D grid. With sequential indicator simulation (SIS), the statistical method in the Schlumberger Petrel software adopted for facies modeling, the proportions of facies used were 4.45% shale, 76.22% sandstone and 19.53% siltstone (Fig. 11a). In addition, to explicitly illustrate the vertical and horizontal facies changes across the reservoir, cross sections of the Charis reservoir were generated (Fig. 11b, c). The interpreted facies from well logs and core reports of the Charis reservoir are interpreted as a channel-fill deposition (massive sandstone beds separated by minor shale and siltstone interbeds), with the sandstones being deposited

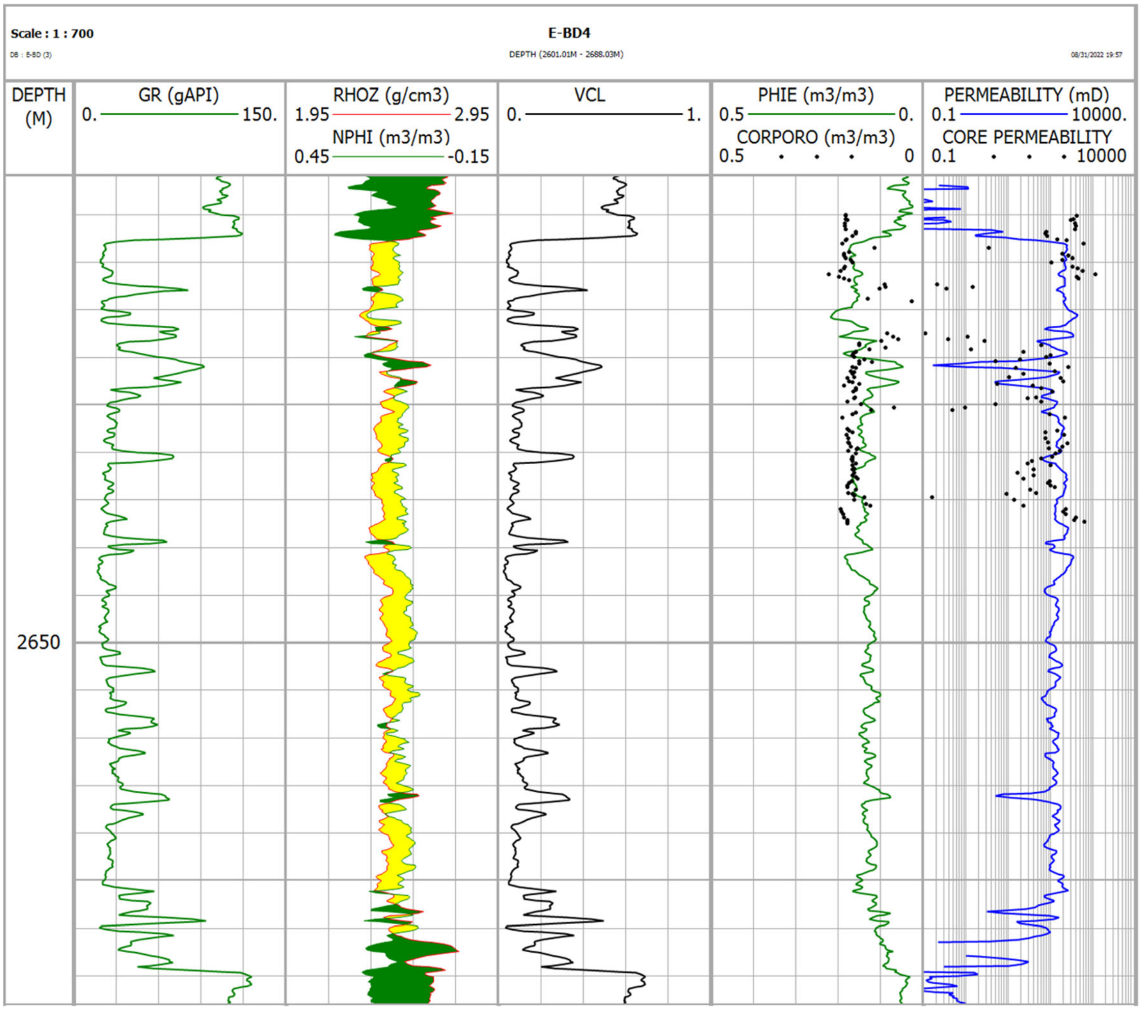

Figure 10. Charis reservoir litho-saturation cross-plots from well E-BD4.

Table 1. Petrophysical properties of Charis reservoir from well log analysis

Curve (unit)	E–BD1	E–BD3	E–BD4
GR (API)	14–101	14–107	17–119
Volume of shale (%)	0.14–77.91	0.11–72.69	0.03–98
PHIE (%)	10.74–21.94	1.53–17.94	0.01–21.67
Permeability (mD)[a]	2.54–203	1.67–679	0.17–431.6
Water saturation (%)	19.51–99.1	7.43–97.12	2–97.77

[a]1 mD = 9.869233 × 10^{-16} m^2

within the confines of a deep-marine channel, firstly as amalgamated inputs, the product of pulses of high-density turbidity currents, followed by deposition in predominantly low sinuosity channels within the overall channel boundaries (Reading & Richards, 1994; Clark & Pickering, 1996).

3D Petrophysical Model

Petrophysical values derived from the Interactive Petrophysics™ software (IP 2021) were upscaled and modeled with the aid of the petrophysical modeling procedure in the Schlumberger Petrel software. The sequential Gaussian simulation algorithm was the statistical method employed for the distribution of the petrophysical parameters (volume of shale, effective porosity, permeability, and water saturation) in the model, cross sections in the

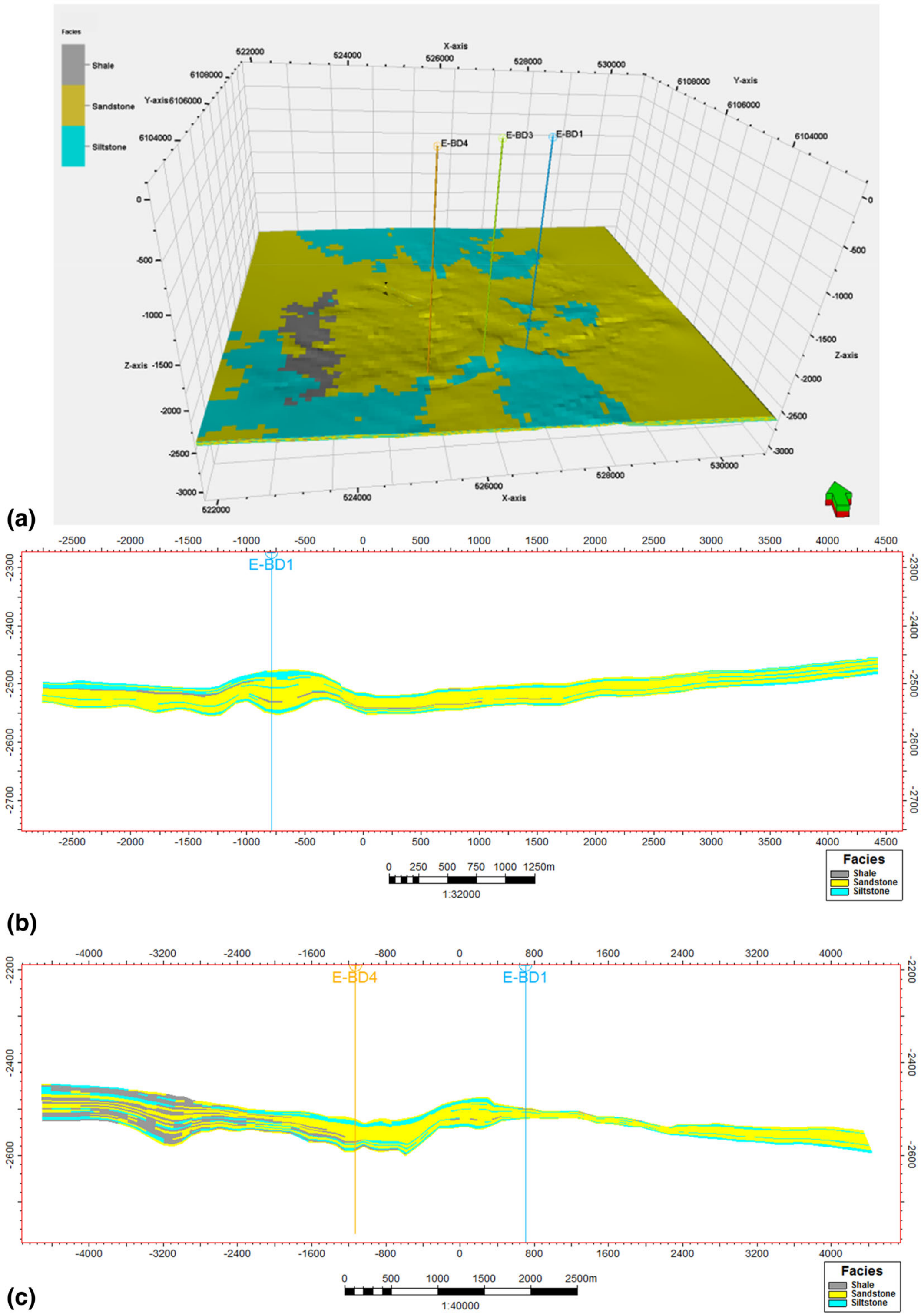

Figure 11. Facies distribution in the Charis reservoir: (**a**) 3D model; (**b**) N–S cross section; (**c**) E–W cross section.

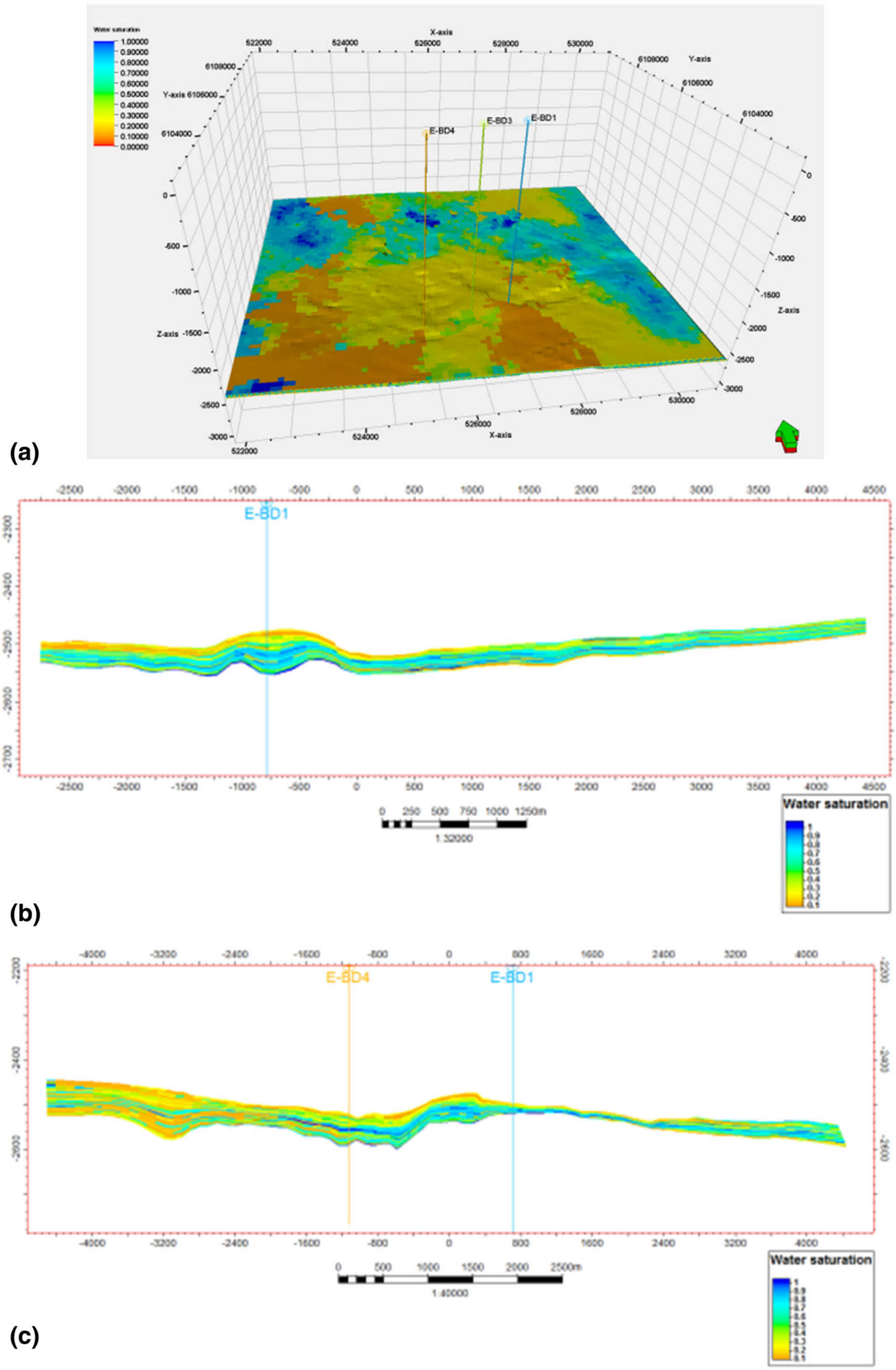

Figure 12. Water saturation distribution in the Charis reservoir: (**a**) 3D model; (**b**) N–S cross section; (**c**) E–W cross section.

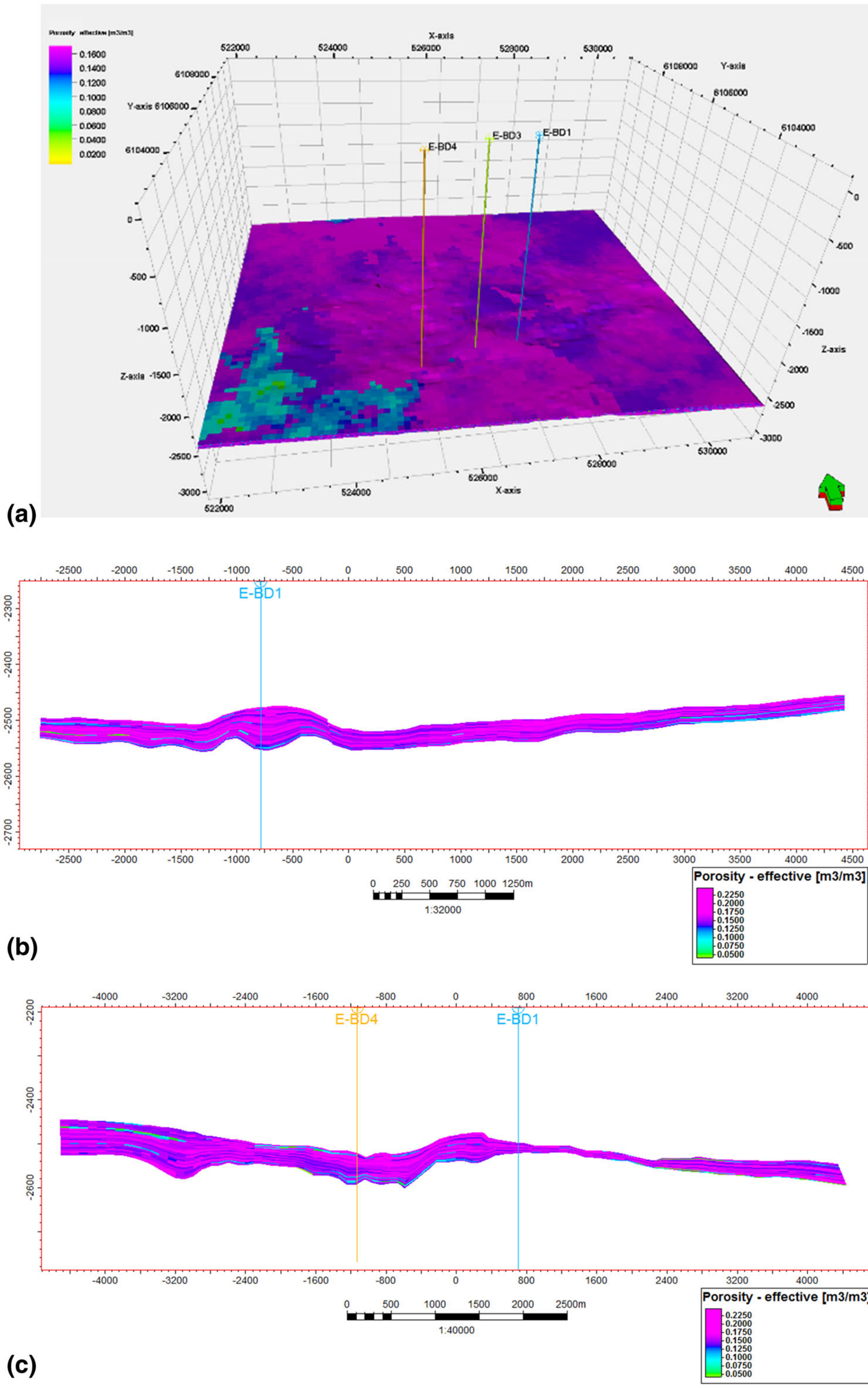

Figure 13. Effective porosity distribution in the Charis reservoir: (**a**) 3D model; (**b**) N–S cross section; (**c**) E–W cross section.

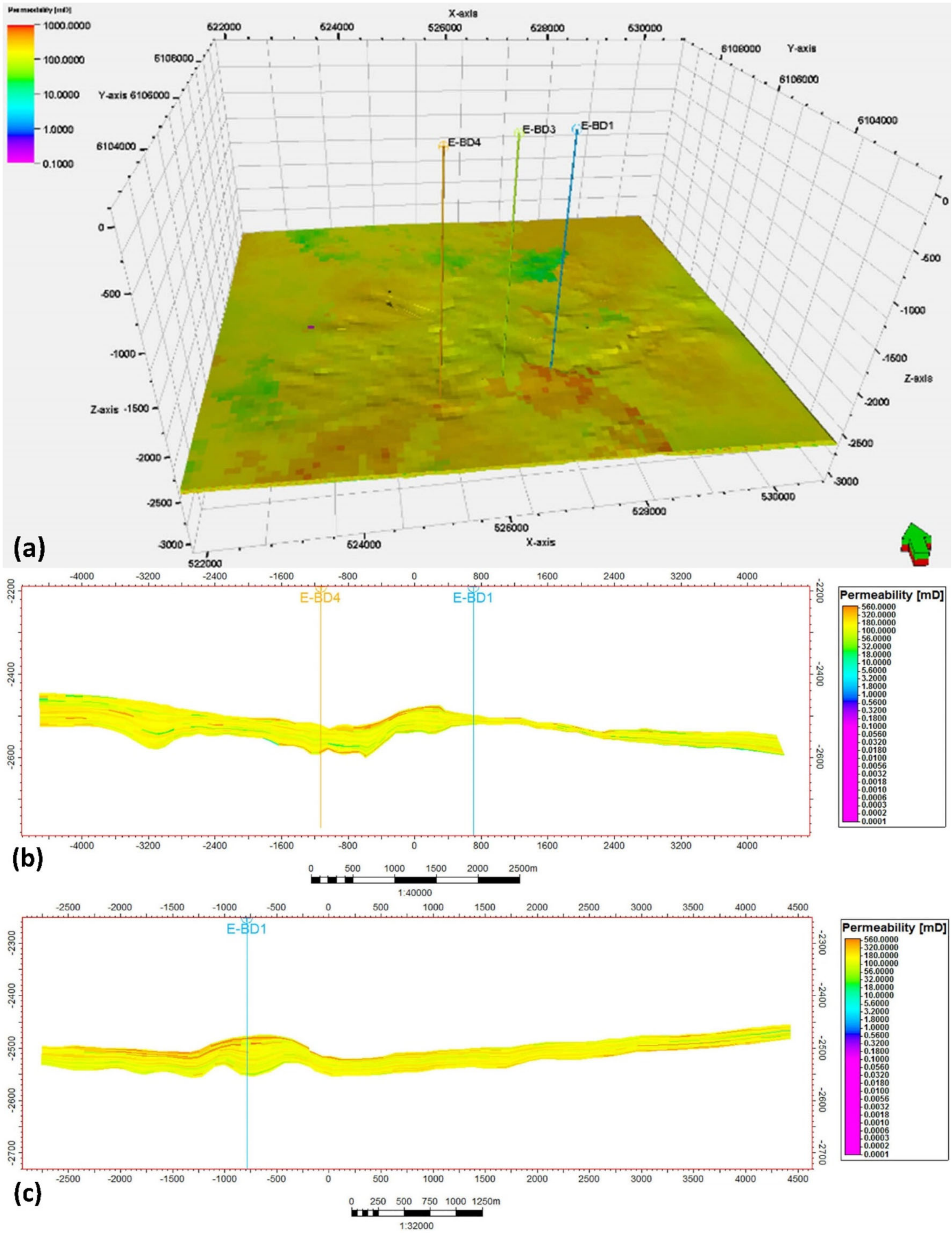

Figure 14. Permeability distribution in the Charis reservoir: (**a**) 3D model; (**b**) N–S cross section; (**c**) E–W cross section.

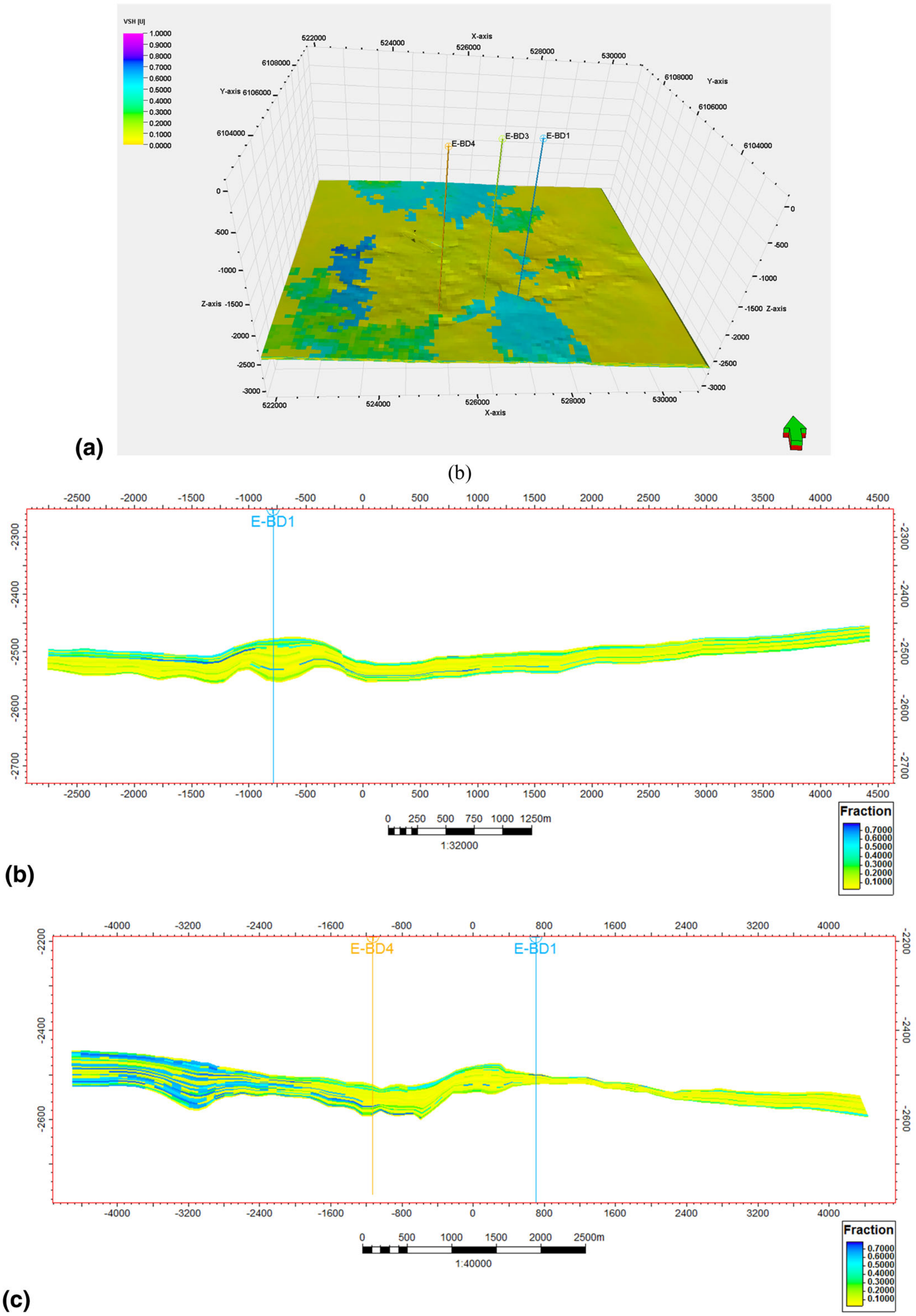

Figure 15. Shale volume distribution in the Charis reservoir: (**a**) 3D model; (**b**) N–S cross section; (**c**) E–W cross section.

Table 2. Classification of reservoir (a) porosity and (b) permeability values (adapted from Levorsen & Berry, 1967)

(a) Porosity (%)	Classification
0–5	Negligible
5–10	Poor reservoir rock
10–15	Fair reservoir rock
15–20	Good reservoir rock
20–25	Very good reservoir rock
(b) Permeability (mD)[a]	Classification
≤ 10.5	Poor to Fair
15–50	Moderate
50–250	Good
250–1000	Very good
> 1000	Excellent

[a]1 mD = 9.869233 × 10^{-16} m^2

Table 3. Calculated CO_2 storage capacity for Charis reservoir with oil phase

Properties	Values
V_p, m^3	184 × 10^6
C_p, kPa^{-1}	5.29 × 10^{-7}
C_w, kPa^{-1}	4.42 × 10^{-7}
C_o, kPa^{-1}	2.02 × 10^{-6}
S_w	0.2
S_o	0.8
Initial pressure, MPa	26.145
Lithostatic pressure, MPa	33.440
ΔP_{max}, MPa	3.951
V_{CO2}, Mt (million tons)	1.62

NS and EW directions were also extracted to recognize both vertical and lateral property distributions in the model (Figs. 12, 13, 14, 15).

The effective porosity model showed values ranging from < 5 to 22%, with permeability values between 100 and 560 mD dominant in the reservoir. The Charis reservoir thus exhibited medium to high porosity and permeability values, with both properties increasing mainly in the northern, southeastern, and central portions of the reservoir. The petrophysical properties of the reservoir tend to be facies-controlled, with the southwestern parts having reduced porosity and permeability values, aligning well with the facies model having a concentration of the siltstone and shale facies in the same area. The *Vsh* model showed low shale fractions in the reservoir, with the reservoir being dominantly composed of clean sands, with water saturation ranging between 10 and 90%. Generally, from the petrophysical and facies characteristics of the Charis reservoir, it is classed as a good reservoir rock (Table 2) (Levorsen and Berry, 1967).

As a potential CO_2 storage site based on proposed parameters (Bachu, 2003; Smith et al., 2012), which serve as the basis for suitable site scoring and ranking, the results showed that the Charis reservoir has good petrophysical characteristics, increasing its potential for CO_2 storage.

Static Storage Capacity Assessment

In the appraisal of a potential CO_2 storage site, estimation of the storage capacity of a reservoir is key, with the two broad methods of estimation (Bachu, 2008; Frailey, 2009; Jin et al., 2012). One method is static capacity estimation (which is simple, straightforward, requires less input data and computational time, and provides a good and useful initial assessment of the reservoir). The other method is numerical simulation (it is dynamic, requires more input data and computational time, but provides more reliable results). The rock and fluid properties, which are the input parameters, are time-dependent in the dynamic estimation but time-independent in the static case (Jin et al., 2012). The most widely used static methods for storage estimation are the compressibility method (van der Meer & Egberts, 2008; Zhou et al., 2008) and volumetric method (Holloway et al., 1996; DOE, 2007; Chadwick et al., 2008). The compressibility method (Eq. 6) which is applied usually for CO_2 storage estimation in confined aquifers and single-phase oil-depleted reservoirs (Goodman et al., 2011; Vulin et al., 2012) was adopted for this study, thus:

$$V_{CO2} = V_p \times \left(C_p + (S_w \times C_w) + (S_o \times C_o)\right) \times \Delta P_{max} \quad (6)$$

where V_{CO2} is calculated volume of CO_2 that can be stored in the reservoir, C is compressibility, S is saturation, and subscripts p, w and o refer to pore space, water, and oil, respectively; ΔP_{max} is maximum allowable pressure increase in the reservoir, which is the difference between the maximum pressure allowed in a system (taken as 90% lithostatic pressure gradient) and the initial pressure of a reservoir. This method assumes that pore space to be filled by the injected CO_2 is dependent on the compressibility of the existing reservoir fluids and the rock (Obdam, 2000; van der Meer & Egberts, 2008; Jin et al., 2012). The fluids and rock compressibility, reservoir pressure, and saturation values were sourced from the well engineering report of the field, with the pore volume gotten from the static model built using the Petrel software. The CO_2 static reservoir capacity computation of Charis reservoir with the presence of an oil phase (virgin oilfield) is presented in Table 3, with input values collected in field units but reported in metric units.

The initial state of the reservoir before oil migration into it was also considered. Equation 6 was then rewritten to eliminate the oil component, thus:

$$V_{CO2} = V_p \times \left(C_p + (S_w \times C_w)\right) \times \Delta Pmax \qquad (7)$$

where V_{CO2} is the calculated volume of CO_2 that can be stored in the reservoir, C is compressibility, S is saturation, subscripts p and w refer to pore space and water; ΔP_{max} is maximum allowable pressure increase in the reservoir, which is the difference between the maximum pressure allowed in the system (taken as 90% lithostatic pressure gradient) and the initial pressure of the reservoir. The reservoir pressure, lithostatic pressure, fluids and rock compressibility values were sourced from the well engineering report of the field, while the pore volume was gotten from the static model built using the Petrel software. The CO_2 static reservoir capacity computation of Charis reservoir fully saturated with water is provided in Table 4, with input values collected in field units and reported in metric units:

Table 4. Calculated CO_2 storage capacity for Charis reservoir fully water saturated

Properties	Values
V_p, m^3	184×10^6
C_p, kPa^{-1}	5.29×10^{-7}
C_w, kPa^{-1}	4.42×10^{-7}
S_w	1
Initial pressure, MPa	26.145
Lithostatic pressure, MPa	33.440
ΔP_{max}, MPa	3.951
V_{CO2}, Mt (million tons)	0.71

SENSITIVITY STUDIES

The sensitivity studies performed on the static capacity estimation of the reservoir included the following:

a. Depleting oilfield at constant initial reservoir pressure (P_i) and increasing water saturation. Using Eq. 6, the results are presented in Table 5 (with V_p, C_p, C_w, C_o and ΔP_{max} being fixed parameters, while S_w increases with decreasing S_o). From Table 5, equal oil and water saturation of 0.5 yielded an estimate of 1.28 Mt CO_2 that can be stored in the reservoir, and while 90% of the reservoir was filled with brine, it was estimated to store 0.82 Mt CO_2. As the oilfield was being depleted and water saturation increased, the volume of CO_2 that can be stored in the field reduced (Fig. 16), this was because water is less compressible than oil.
b. Depleting oilfield and depressurization—initial pressure was dropped to bubble point pressure (Pb) while increasing water saturation in the system (ΔP_{max} is the difference between the maximum pressure allowed in the system (taken as 90% lithostatic pressure gradient) and the bubble point pressure of the reservoir; V_p, C_p, C_w, C_o, P_b and ΔP_{max} are fixed parameters, while S_w increased with decreasing S_o). Using Eq. 6, the results are presented in Table 6 and Figure 17. In a depleting oilfield at bubble point pressure, the total volume of CO_2 that can be stored also reduces with increasing water satu-

Table 5. Depleting oilfield (increasing S_w and reducing S_o) at constant initial reservoir pressure (P_i)

V_p, m^3	C_p, kPa^{-1}	C_w, kPa^{-1}	C_o, kPa^{-1}	S_w	S_o	ΔP_{max}, MPa	V_{CO2}, Mt (million tons)
184×10^6	5.29×10^{-7}	4.42×10^{-7}	2.02×10^{-6}	0.5	0.5	3.951	1.28
184×10^6	5.29×10^{-7}	4.42×10^{-7}	2.02×10^{-6}	0.6	0.4	3.951	1.17
184×10^6	5.29×10^{-7}	4.42×10^{-7}	2.02×10^{-6}	0.7	0.3	3.951	1.05
184×10^6	5.29×10^{-7}	4.42×10^{-7}	2.02×10^{-6}	0.8	0.2	3.951	0.94
184×10^6	5.29×10^{-7}	4.42×10^{-7}	2.02×10^{-6}	0.9	0.1	3.951	0.82

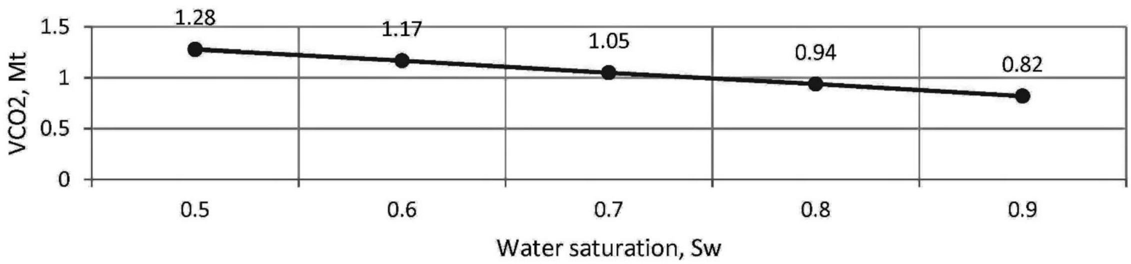

Figure 16. CO_2 static capacity estimate for depleting oilfield at initial reservoir pressure (P_i).

Table 6. Depleting oilfield (increasing S_w and reducing S_o) and depressurization (reservoir depressurized to bubble point pressure P_b)

V_p, m^3	C_p, kPa^{-1}	C_w, kPa^{-1}	C_o, kPa^{-1}	S_w	S_o	*Bubble point pressure P_b*, MPa	ΔP_{max}, MPa	V_{CO2}, Mt (million tons)
184×10^6	5.29×10^{-7}	4.42×10^{-7}	2.02×10^{-6}	0.5	0.5	20.86	9.232	2.99
184×10^6	5.29×10^{-7}	4.42×10^{-7}	2.02×10^{-6}	0.6	0.4	20.86	9.232	2.72
184×10^6	5.29×10^{-7}	4.42×10^{-7}	2.02×10^{-6}	0.7	0.3	20.86	9.232	2.45
184×10^6	5.29×10^{-7}	4.42×10^{-7}	2.02×10^{-6}	0.8	0.2	20.86	9.232	2.19
184×10^6	5.29×10^{-7}	4.42×10^{-7}	2.02×10^{-6}	0.9	0.1	20.86	9.232	1.92

ration, though the volumes at each water saturation point are more than twice the corresponding values at initial reservoir pressure. Therefore, reduction in reservoir pressure will give increasing volume of CO_2 that can be stored in a reservoir.

c. Non-depleting oilfield with continued depressurization—constant water saturation and reservoir pressure at 1000 psi.[1] At bubble point pressure, the first bubble of natural gas begins to come out of solution, and as the reservoir pressure continues to decrease, more gas comes out of solution to form a gas cap. The gas component was therefore introduced into Eq. 6 to give:

$$V_{CO2} = V_p \times \left(C_p + (S_w \times C_w) + (S_o \times C_o) + \left(S_g \times C_g\right)\right) \times \Delta Pmax \quad (8)$$

where V_{CO2} is the calculated volume of CO_2 that can be stored in the reservoir, C is compressibility, S is saturation, and subscripts *p, w, o and g* refer to pore space, water, oil and gas, respectively; ΔP_{max} is the maximum allowable pressure increase in the reservoir, which is the difference between the maximum pressure allowed in the system (taken as 90% lithostatic pressure gradient) and 1000 psi (6.895 MPa), with V_p, C_p, C_w, C_o, C_g, P_b, S_w, new reservoir pressure (1000 psi) and ΔP_{max} are fixed parameters, while S_g increases with decreasing S_o. The results are presented in Table 7 and Figure 18. The depressurization case in Table 7 and Figure 18 shows that as gas cap formed below bubble point pressure, the volume of CO_2 that can be stored increased with increasing gas saturation. This is because gas is more compressible than oil and water.

CONCLUSIONS

Carbon capture, utilization and storage remain an important and essential technology for countries and industries to reduce worldwide environmental change, with underground storage of carbon dioxide in geological formations a core of carbon sequestration, especially in non-renewable energy-centered nations. Developing a robust geological model of underground formations is paramount for CO_2 storage site appraisal, to deduce their facies and petrophysical properties.

The investigated Charis reservoir as a potential CO_2 storage site is a sandstone reservoir with mean effective porosity of 13.92% and dominant permeability values of 100–560 mD, with both properties

[1] 1 psi = 6.8947572932 kPa.

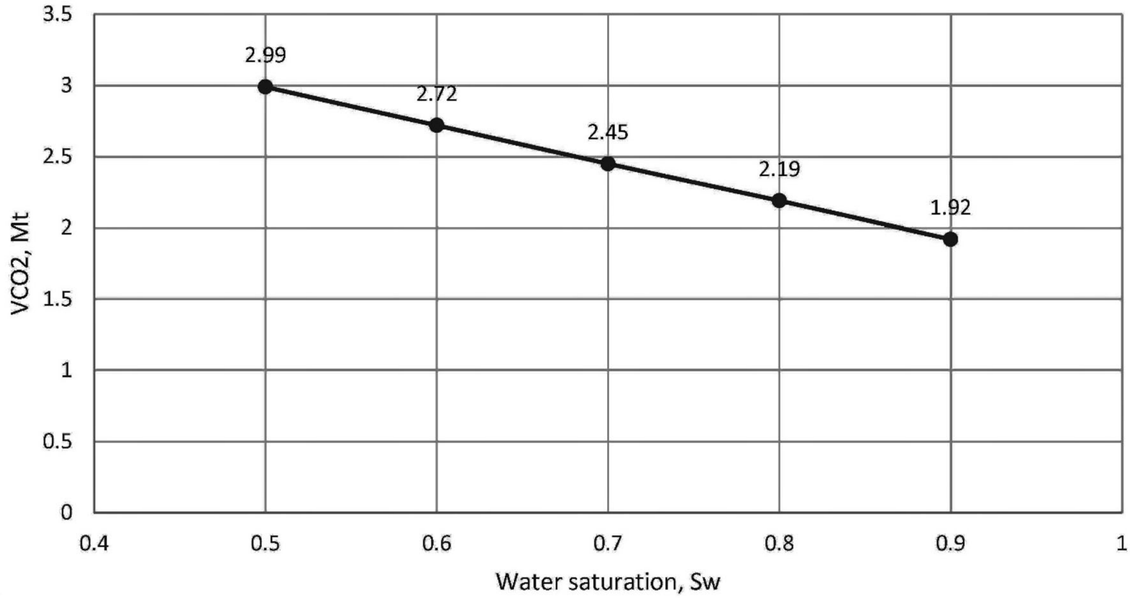

Figure 17. CO_2 static capacity estimate for depleting oilfield at bubble point pressure (P_b).

Table 7. Non-depleting oilfield (constant S_w) at 1000 psi (increasing gas saturation (S_g) and decreasing oil saturation (S_o)

V_p, m^3	C_p, kPa^{-1}	C_w, kPa^{-1}	C_o, kPa^{-1}	Cg, kPa^{-1}	S_w	S_o	S_g	New reservoir pressure (1000 psi*), MPa	ΔP_{max}, MPa	V_{CO2}, Mt (million tons)
184×10^6	5.29×10^{-7}	4.42×10^{-7}	2.02×10^{-6}	2.54×10^{-6}	0.5	0.4	0.1	6.895	23.201	7.74
184×10^6	5.29×10^{-7}	4.42×10^{-7}	2.02×10^{-6}	2.54×10^{-6}	0.5	0.3	0.2	6.895	23.201	7.96
184×10^6	5.29×10^{-7}	4.42×10^{-7}	2.02×10^{-6}	2.54×10^{-6}	0.5	0.2	0.3	6.895	23.201	8.18
184×10^6	5.29×10^{-7}	4.42×10^{-7}	2.02×10^{-6}	2.54×10^{-6}	0.5	0.1	0.4	6.895	23.201	8.40

*1 psi = 6.8947572932 kPa

increasing in the reservoir's northern, southeastern and central portions. The southwestern area with siltstone and shale facies has reduced porosity and permeability, making the petrophysical properties of the reservoir facies controlled. The volume of shale model shows that the reservoir is composed of clean sands and water saturation ranging between 10 and 90%. The reservoir is suitable for CO_2 storage based on its porosity and permeability.

As a virgin oilfield, it is estimated the reservoir can sequester around 1.62 Mt (million tons) of CO_2, and 0.71 Mt of CO_2 with the reservoir fully water-saturated, based on only the static storage volume estimate of the reservoir. Increasing reservoir water saturation (a depleting oilfield at constant initial reservoir pressure) decreases CO_2 storage capacity of the reservoir because water is less compressible than oil. Oil depletion (increasing water saturation) at bubble point pressure is also attended with decreasing CO_2 storage capacity, although the total CO_2 volume that can be stored is more than twice the volume at each water saturation level while the reservoir was at initial reservoir pressure. The oilfield, not under depletion and at 1000 psi, with a gas cap and water saturation of 50%, significantly increases CO_2 storage volume because gas is more compressible than oil and water.

Further credence can be given to the reservoir and seal in the field because it has held and kept hydrocarbon in place in the geologic past, and the

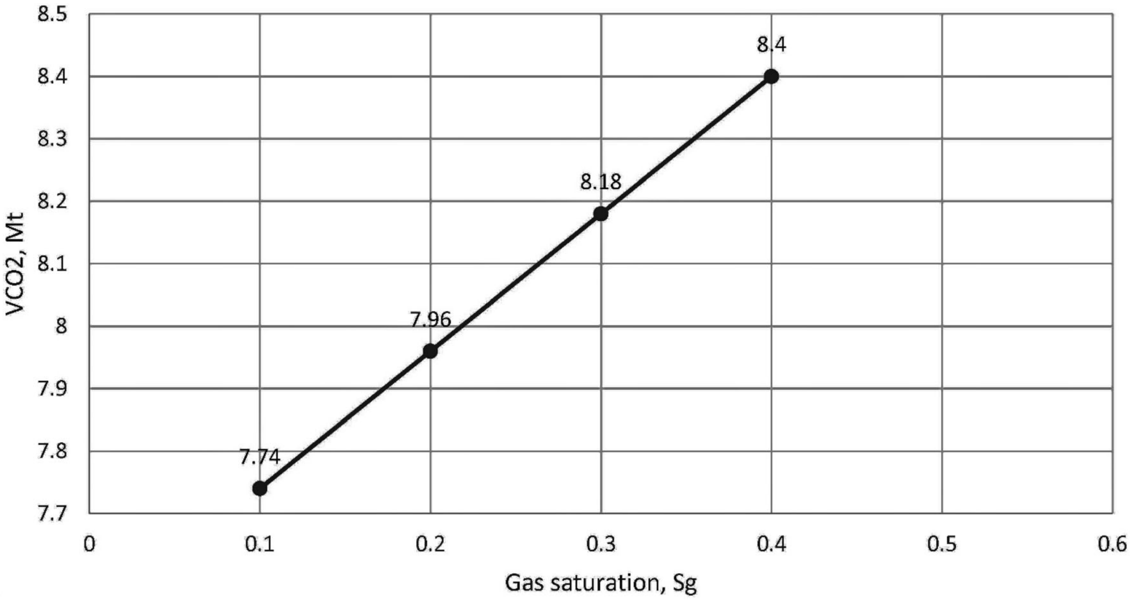

Figure 18. CO_2 static capacity estimate for non-depleting oilfield at 1000 psi (1 psi = 6.8947572932 kPa).

field has been produced. The presence of residual oil will also increase the volume of CO_2 that can be stored in the reservoir. This study presents a detailed investigation into an oilfield within the Bredasdorp Basin as a potential CO_2 storage site and can be used to compare the well-explored gas fields in the basin, it is also the primary input for dynamic simulation of the field.

ACKNOWLEDGMENTS

The authors are grateful to the Petroleum Agency of South Africa (PASA) for providing the data and well reports for the study. They also thank Synergy LR Company and Schlumberger Limited for providing access to Interactive Petrophysics (IP 2021 (4.7)) and Petrel software, respectively, used for data analysis. Mrs Leah Bailey of Schlumberger Limited is particularly appreciated for her help during the data analysis.

FUNDING

Open access funding provided by University of the Western Cape. The funding provided by the National Institute for Theoretical and Computational Sciences (NITheCS) South Africa toward this research is acknowledged.

DECLARATIONS

Conflict of Interest The authors declare that they have no known competing financial interests or personal relationships that could have appeared to influence the work reported in this paper.

OPEN ACCESS

REFERENCES

Abbaszadeh, M., Fujii, H., & Fujimoto, F. (1996). Permeability prediction by hydraulic flow units-theory and applications. *SPE Formation Evaluation, 11*(04), 263–271.

Abdel-Fattah, M. I., Metwalli, F. I., & Mesilhi, E. S. I. (2018). Static reservoir modeling of the Bahariya reservoirs for the oilfields development in South Umbarka area, Western Desert Egypt. *Journal of African Earth Sciences, 138*, 1–13.

Abdullah, E. A., Abdelmaksoud, A., & Hassan, M. A. (2021). Application of 3D static modelling in reservoir characterization: a case study from Qishn formation in Sharyoof oil field, Masila Basin, Yemen. *Acta Geologica Sinica - English Edition, 96*(1), 348–368.

Acho, C. B. (2015). Assessing Hydrocarbon Potential in Cretaceous Sediments in the Western Bredasdorp Sub-basin in the Outeniqua Basin South Africa [Unversity of the Western Cape, South Africa]. In *Thesis* (Issue July). 3/Record/com.-mandumah.search.

Adelu, A. O., Aderemi, A. A., Akanji, A. O., Sanuade, O. A., Kaka, S. L. I., Afolabi, O., Olugbemiga, S., & Oke, R. (2019). Application of 3D static modeling for optimal reservoir characterization. *Journal of African Earth Sciences, 152*, 184–196.

Alcalde, J., Heinemann, N., James, A., Bond, C. E., Ghanbari, S., Mackay, E. J., Haszeldine, R. S., Faulkner, D. R., Worden, R. H., & Allen, M. J. (2021). A criteria-driven approach to the CO2 storage site selection of East Mey for the acorn project in the North Sea. *Marine and Petroleum Geology, 133*, 105309.

Alcalde, J., Heinemann, N., Mabon, L., Worden, R. H., de Coninck, H., Robertson, H., Maver, M., Ghanbari, S., Swennenhuis, F., Mann, I., Walker, T., Gomersal, S., Bond, C. E., Allen, M. J., Haszeldine, R. S., James, A., Mackay, E. J., Brownsort, P. A., Faulkner, D. R., & Murphy, S. (2019). Acorn: Developing full-chain industrial carbon capture and storage in a resource- and infrastructure-rich hydrocarbon province. *Journal of Cleaner Production, 233*, 963–971.

Ali, A. M., Radwan, A. E., Abd El-Gawad, E. A., & Abdel-Latief, A. S. A. (2021). 3D integrated structural, facies and petrophysical static modeling approach for complex sandstone reservoirs: a case study from the coniacian-santonian matulla formation, July Oilfield, Gulf of Suez. *Egypt. Natural Resources Research, 31*(1), 385–413.

Ali, M., Abdelhady, A., Abdelmaksoud, A., Darwish, M., & Essa, M. A. (2020a). 3D static modeling and petrographic aspects of the albian/cenomanian reservoir, Komombo Basin Upper Egypt. *Natural Resources Research, 29*(2), 1259–1281.

Ali, M., Abdelmaksoud, A., Essa, M. A., Abdelhady, A., & Darwish, M. (2020b). 3D structural, facies and petrophysical modeling of C member of six hills formation, Komombo Basin Upper Egypt. *Natural Resources Research, 29*(4), 2575–2597.

Amaefule, J. O., Altunbay, M., Tiab, D., Kersey, D. G., & Keelan, D. K. (1993). Enhanced reservoir description: using core and log data to identify hydraulic (flow) units and predict permeability in uncored intervals/wells. *SPE Annual Technical Conference and Exhibition*.

Ampomah, W., Balch, R. S., Cather, M., Will, R., Gunda, D., Dai, Z., & Soltanian, M. R. (2017). Optimum design of CO2 storage and oil recovery under geological uncertainty. *Applied Energy, 195*, 80–92.

Anastassia, M., Fredrick, O., & Malcolm, W. (2010). The future of Carbon Capture and Storage (CCS) in Nigeria. *Science World Journal, 4*(3), 1–6.

Archie, G. E. (1942). The electrical resistivity log as an aid in determining some reservoir characteristics. *Transactions of the AIME, 146*(01), 54–62.

Asquith, G. B., & Gibson, C. R. (1982). *Basic well log analysis for geologists* (Vol. 3). American Association of Petroleum Geologists Tulsa.

Ayodele, O. L., Chatterjee, T. K., & Opuwari, M. (2021). Static reservoir modeling using stochastic method: A case study of the cretaceous sequence of Gamtoos Basin, Offshore, South Africa. *Journal of Petroleum Exploration and Production Technology, 11*(12), 4185–4200.

Bachu, S. (2008). Comparison between methodologies recommended for estimation of CO2 storage capacity in geological media. *Carbon Sequestration Leadership Forum, Phase III Report*.

Bachu, S. (2003). Screening and ranking of sedimentary basins for sequestration of CO2 in geological media in response to climate change. *Environmental Geology, 44*(3), 277–289.

Bandilla, K. W., Guo, B., & Celia, M. A. (2019). A guideline for appropriate application of vertically-integrated modeling approaches for geologic carbon storage modeling. *International Journal of Greenhouse Gas Control, 91*, 102808.

Boden, T. A., Marland, G., & Andres, R. J. (2011). *Global, Regional, and National Fossil-Fuel CO2 Emissions, 1751–2008 (Version 2011)*. Environmental System Science Data Infrastructure for a Virtual Ecosystem (ESS-DIVE)(United States); Carbon Dioxide Information Analysis Center (CDIAC), Oak Ridge National Laboratory (ORNL), Oak Ridge, TN (United States).

Broad, D. S., Jungslager, E. H. A., McLachlan, I. R., Roux, J., & Van der Spuy, D. (2012). South Africa's offshore Mesozoic basins. In *Regional Geology and Tectonics: Phanerozoic Passive Margins, Cratonic Basins and Global Tectonic Maps* (pp. 534–564). Elsevier.

Brown, L. F. J., Benson, J. M., Brink, G. J., Doherty, S., Jollands, A., Jungslager, E. H. A., Keenan, J. H. G., Muntingh, A., & van Wyk, N. J. S. (1995). Sequence Stratigraphy in Offshore South African Divergent Basins-Front Matter. *SG 41*, 1–18.

Bui, M., Adjiman, C. S., Bardow, A., Anthony, E. J., Boston, A., Brown, S., Fennell, P. S., Fuss, S., Galindo, A., Hackett, L. A., Hallett, J. P., Herzog, H. J., Jackson, G., Kemper, J., Krevor, S., Maitland, G. C., Matuszewski, M., Metcalfe, I. S., & Petit, C. (2018). Carbon capture and storage (CCS): The way forward. *Energy and Environmental Science, 11*(5), 1062–1176.

Chabangu, N., Beck, B., Hicks, N., Botha, G., Viljoen, J., Davids, S., & Cloete, M. (2014a). The investigation of CO2 storage potential in the Zululand Basin in South Africa. *Energy Procedia, 63*, 2789–2799.

Chabangu, N., Beck, B., Hicks, N., Viljoen, J., Davids, S., & Cloete, M. (2014b). The investigation of CO2 storage potential in the Algoa basin in South Africa. *Energy Procedia, 63*, 2800–2810.

Chadwick, A., Arts, R. J., Bernstone, C., May, F., Thibeau, S., & Zweigel, P. (2008). *Best practice for the storage of CO2 in saline aquifers-observations and guidelines from the SACS and CO2STORE projects (Vol. 14)*.

Clark, J. D., & Pickering, K. T. (1996). Architectural elements and growth patterns of submarine channels: application to hydrocarbon exploration. *AAPG Bulletin, 80*(2), 194–220.

Cloete, M. (2010). *ATLAS on geological storage of carbon dioxide in South Africa. January 2010*, 1–61. http://www.sacccs.org.za/wp-content/uploads/2010/11/Atlas.pdf.

Davies, C. P. N. (1997). Hydrocarbon evolution of the Bredasdorp Basin, offshore South Africa: from source to reservoir. *Thesis*, *December*, 1–1123. http://scholar.sun.ac.za/handle/10019.1/4936.

Dingle, R. V. (1983). *Mesozoic and Tertiary geology of southern Africa/R.V. Dingle, W.G. Siesser, A.R. Newton* W. G. Siesser & A. R. Newton (eds.). A.A. Balkema; Distributed in the U.S.A. & Canada by M.B.S.

DOE. (2007). *Carbon sequestration atlas of the United States and Canada: Appendix A—Methodology for development of carbon sequestration capacity estimates; report on the 2007 Carbon Sequestration Atlas of the United States and Canada (Atlas I)* (D.o.E. National energy Technology Laboratory (ed.); pp. 1–90). https://doi.org/10.12987/9780300185294-003.

El Khadragy, A. A., Eysa, E. A., Hashim, A., & Abd El Kader, A. (2017). Reservoir characteristics and 3D static modelling of the Late Miocene Abu Madi Formation, onshore Nile Delta Egypt. *Journal of African Earth Sciences, 132*, 99–108.

Frailey, S. (2009). Methods for Estimating CO(2) Storage in Saline Reservoirs. *Energy Procedia, 1*, 2769–2776.

Ghanbari, S., Mackay, E. J., Heinemann, N., Alcalde, J., James, A., & Allen, M. J. (2020). Impact of CO2 mixing with trapped hydrocarbons on CO2 storage capacity and security: A case study from the Captain aquifer (North Sea). *Applied Energy, 278*, 115634.

Goodman, A., Hakala, A., Bromhal, G., Deel, D., Rodosta, T., Frailey, S., Small, M., Allen, D., Romanov, V., & Fazio, J. (2011). US DOE methodology for the development of geologic storage potential for carbon dioxide at the national and regional scale. *International Journal of Greenhouse Gas Control, 5*(4), 952–965.

Haelbich, I. W., Fitch, F. J., & Miller, J. A. (1983). *Dating the Cape orogeny*. The Geological Society of South Africa. http://inis.iaea.org/search/search.aspx?orig_q=RN:17008619.

Hendricks, M. Y. (2019). *Provenance and Depositional Environments of Early Cretaceous Sediments in the Bredasdorp Sub-Basin, Offshore South Africa: an Integrated Approach*. University of the Western Cape.

Hietkamp, S., Engelbrecht, A., Scholes, B., & Golding, A. (2004). Carbon capture and storage in South Africa. *Transport, 40*, 22.

Holloway, S., Rochelle, C., Bateman, K., Pearce, J., Baily, H., & Metcalfe, R. (1996). *The underground disposal of carbon dioxide*. British Geological Survey.

IPCC. (2018). IPCC report Global warming of 1.5°C. *Global Warming of 1.5°C. An IPCC Special Report on the Impacts of Global Warming of 1.5°C above Pre-Industrial Levels and Related Global Greenhouse Gas Emission Pathways, in the Context of Strengthening the Global Response to the Threat of Climate Change, 2*(October), 17–20. www.environmentalgraphiti.org.

Jin, M., Pickup, G., Mackay, E., Todd, A., Sohrabi, M., Monaghan, A., & Naylor, M. (2012). Static and dynamic estimates of CO2-storage capacity in two saline formations in the UK. *SPE Journal, 17*(4), 1108–1118.

Jungslager, E. H. A. (1999). Petroleum habitats of the Atlantic margin of South Africa. *Geological Society, London, Special Publications, 153*(1), 153–168.

Kadkhodaie-Ilkhchi, R., Rezaee, R., Moussavi-Harami, R., & Kadkhodaie-Ilkhchi, A. (2013). Analysis of the reservoir electrofacies in the framework of hydraulic flow units in the Whicher Range Field, Perth Basin, Western Australia. *Journal of Petroleum Science and Engineering, 111*, 106–120.

Kempka, T., Norden, B., Ivanova, A., & Löth, S. (2017). Revising the static geological reservoir model of the upper triassic stuttgart formation at the ketzin pilot site for CO2 storage by integrated inverse modelling. *Energies, 10*(10), 1559.

Kumar, A., Noh, M. H., Ozah, R. C., Pope, G. A., Bryant, S. L., Sepehrnoori, K., & Lake, L. W. (2005). Reservoir simulation of CO_2 storage in aquifers. *SPE Journal, 10*(03), 336–348.

Larionov, V. V. (1969). Borehole radiometry. *Nedra, Moscow, 127*, 813.

Levorsen, A. I., & Berry, F. A. F. (1967). Geology of petroleum LK. In *A Series of books in geology TA-TT*(2nd ed.). W.H. Freeman and Co. https://uwc.on.worldcat.org/oclc/490246406.

Magoba, M., & Opuwari, M. (2017). An Interpretation of core and Wireline logs for the Petrophysical evaluation of Upper Shallow Marine reservoirs of the Bredasdorp Basin, Offshore South Africa Moses Magoba and Mimonitu Opuwari. *European Geosciences Union General Assembly 2017*. www.egu.eu.

Mcmillan, I. K., Brink, G. I., Broad, D. S., & Maier, J. J. (1997). Chapter 13 late Mesozoic sedimentary basins off the south coast of South Africa. In R. C. Selley (Ed.), *African Basins* (Vol. 3, pp. 319–376). Elsevier. https://doi.org/10.1016/S1874-5997(97)80016-0.

Meer, L. V., & der. (1995). The CO2 storage efficiency of aquifers TN0 institute of applied geoscience. *Energy Conversion and Management, 36*(6), 513–518.

Nabawy, B. S., & Al-Azazi, N. A. S. A. (2015). Reservoir zonation and discrimination using the routine core analyses data: The upper Jurassic Sab'atayn sandstones as a case study, Sab'atayn basin. *Yemen. Arabian Journal of Geosciences, 8*(8), 5511–5530.

Nfor, N. E. (2011). *Sequence stratigraphic characterisation of petroleum reservoirs in block 11b / 12b of the Southern Outeniqua Basin*.

Niri, M. E. (2018). *3D and 4D Seismic data integration in static and dynamic reservoir modeling: A review*. *8*(2), 38–56. https://doi.org/10.22078/jpst.2017.2320.1407.

Obdam, A. (2000). Aquifer storage capacity of CO2. *TNO-Built Environment & Geosciences, Utrecht, The Netherlands*.

Ojo, A. C., & Tse, A. C. (2016). Geological characterisation of depleted oil and gas reservoirs for carbon sequestration potentials in a field in the Niger Delta, Nigeria. *Journal of Applied Sciences and Environmental Management, 20*(1), 45.

Okoli, A. E., Agbasi, O. E., Lashin, A. A., & Sen, S. (2021). Static reservoir modeling of the eocene clastic reservoirs in the Q-Field, Niger Delta Nigeria. *Natural Resources Research, 30*(2), 1411–1425.

Opuwari, M., Afolayan, B., Mohammed, S., Amaechi, P. O., Bareja, Y., & Chatterjee, T. (2022). Petrophysical core-based zonation of OW oilfield in the Bredasdorp Basin South Africa. *Scientific Reports, 12*(1), 1–19.

Opuwari, M., Mohammed, S., & Ile, C. (2021). Determination of reservoir flow units from core data: A case study of the lower cretaceous sandstone reservoirs, Western Bredasdorp Basin Offshore in South Africa. *Natural Resources Research, 30*(1), 411–430.

Othman, A. A. A., Fathy, M., Othman, M., & Khalil, M. (2021). 3D static modeling of the Nubia Sandstone reservoir, gamma offshore field, southwestern part of the Gulf of Suez. *Egypt. Journal of African Earth Sciences, 177*, 104160. https://doi.org/10.1016/j.jafrearsci.2021.104160.

Parker, I. (2014). *Petrophysical evaluation of sandstone reservoirs of the Central Bredasdorp Basin , Block 9 , Offshore South Africa By Irfaan Parker*.

Perez, H. H., Datta-Gupta, A., & Mishra, S. (2003). The role of electrofacies, lithofacies, and hydraulic flow units in permeability predictions from well logs: a comparative analysis using classification trees. *SPE Annual Technical Conference and Exhibition*.

Petroleum Agency of South Africa. (2017). *Petroleum Exploration in South Africa Brochure Information and Opportunities*. 48. http://info.matchdeck.com/hubfs/PASA_Exploration_Opportunities_in_SA.pdf.

Radwan, A. E., Wood, D. A., Mahmoud, M., & Tariq, Z. (2022b). Chapter Twelve - Gas adsorption and reserve estimation for conventional and unconventional gas resources. In D. A. Wood & J. B. T.-S. G. for N. G. S. S. Cai (Eds.), *The Fundamentals and Sustainable Advances in Natural Gas Science and Eng* (Vol. 2, pp. 345–382). Gulf Professional Publishing. https://doi.org/10.1016/B978-0-323-85465-8.00004-2.

Radwan, A. A., Abdelwahhab, M. A., Nabawy, B. S., Mahfouz, K. H., & Ahmed, M. S. (2022a). Facies analysis-constrained geophysical 3D-static reservoir modeling of Cenomanian units in the Aghar Oilfield (Western Desert, Egypt): Insights into paleoenvironment and petroleum geology of fluviomarine systems. *Marine and Petroleum Geology, 136*, 105436.

Radwan, A. E., Nabawy, B. S., Kassem, A. A., & Hussein, W. S. (2021). Implementation of rock typing on waterflooding process during secondary recovery in oil reservoirs: A case study, El Morgan Oil Field, Gulf of Suez Egypt. *Natural Resources Research, 30*(2), 1667–1696.

Rahimi, M., & Riahi, M. A. (2020). Static reservoir modeling using geostatistics method: A case study of the Sarvak Formation in an offshore oilfield. *Carbonates and Evaporites, 35*(2), 1–13.

Reading, H. G., & Richards, M. (1994). Turbidite systems in deep-water basin margins classified by grain size and feeder system 1. *AAPG Bulletin, 78*(5), 792–822.

Saadu, Y. K., & Nwankwo, C. N. (2018). Petrophysical evaluation and volumetric estimation within Central swamp depobelt, Niger Delta, using 3-D seismic and well logs. *Egyptian Journal of Petroleum, 27*(4), 531–539.

Sarhan, M. A., Hassan, T., & Ali, A. S. (2022). 3D static reservoir modelling of Abu Madi paleo-valley in Baltim Field, Offshore Nile Delta Basin Egypt. *Petroleum Research, 7*(4), 473–485.

Shariatipour, S. M., Mackay, E. J., & Pickup, G. E. (2016). An engineering solution for CO2 injection in saline aquifers. *International Journal of Greenhouse Gas Control, 53*, 98–105.

Smith, M., Campbell, D., Mackay, E., & Polson, D. (2012). *CO2 Aquifer Storage Site Evaluation and Monitoring (CASSEM) Understanding the challenges of CO2 storage: results of the CASSEM Project*.

Smith, R. M. H. (1990). Alluvial paleosols and pedofacies sequences in the Permian Lower Beaufort of the southwestern Karoo Basin, South Africa. *Journal of Sedimentary Research, 60*(2), 258–276.

South Africa Department of Energy. (2009). *Digest of South African energy statistics*. Doi:https://doi.org/10.1016/j.infsof.2008.09.005.

Teletzke, G. F., & Lu, P. (2013). Guidelines for reservoir modeling of geologic CO2 storage. *Energy Procedia, 37*, 3936–3944.

Tibane, L. V., Pöllmann, H., Ndongani, F. L., Landman, B., & Altermann, W. (2021). Evaluation of the lithofacies, petrography, mineralogy, and geochemistry of the onshore Cretaceous Zululand Basin in South Africa for geological CO2 storage. *International Journal of Greenhouse Gas Control, 109*, 103364.

Tsuji, T., Matsuoka, T., Kadir, W. G. A., Hato, M., Takahashi, T., Sule, M. R., Kitamura, K., Yamada, Y., Onishi, K., Widarto, D. S., Sebayang, R. I., Prasetyo, A., Priyono, A., Ariadji, T., Sapiie, B., Widianto, E., & Asikin, A. R. (2014). Reservoir characterization for site selection in the Gundih CCS project. *Indonesia. Energy Procedia, 63*, 6335–6343.

UNFCCC. (2015). Adoption of the Paris agreement. In *Proposal by the President* (Vol. 282). https://doi.org/10.1126/science.364.6435.39-f.

van der Meer, L., & Egberts, P. J. P. (2008). A General Method for Subsurface CO2 Storage Capacity Calculations. In *Offshore Technology Conference* (OTC-19309-MS). https://doi.org/10.4043/19309-MS.

Viljoen, J. H. A., Stapelberg, F. D. J., & Cloete, M. (2010). *Technical Report on the Geological Storage of Carbon Dioxide*.

Vincent, C. J., Hicks, N., Arenstein, G., Tippmann, R., Van Der Spuy, D., Viljoen, J., Davids, S., Roos, M., Cloete, M., Beck, B., Nell, L., Arts, R., Holloway, S., Surridge, T., & Pearce, J. (2013). The proposed CO2 Test Injection project in South Africa. *Energy Procedia, 37*, 6489–6501.

Vulin, D., Kurevija, T., & Kolenkovic, I. (2012). The effect of mechanical rock properties on CO2 storage capacity. *Energy, 45*(1), 512–518. https://doi.org/10.1016/j.energy.2012.01.059.

Winkler, H., Spalding-Fecher, R., Mwakasonda, S., & Davidson, O. (2002). Sustainable development policies and measures: starting from development to tackle climate change. *Building on the Kyoto Protocol Options for Protecting the Climate, 2*, 61–87.

Würdemann, H., Möller, F., Kühn, M., Heidug, W., Christensen, N. P., Borm, G., & Schilling, F. R. (2010). CO2SINK-From site characterisation and risk assessment to monitoring and verification: One year of operational experience with the field laboratory for CO2 storage at Ketzin, Germany. *International Journal of Greenhouse Gas Control, 4*(6), 938–951.

Yan, J., & Zhang, Z. (2019). Carbon Capture, Utilization and Storage (CCUS). *Applied Energy, 235*, 1289–1299.

Yelebe, Z. R., & Samuel, R. J. (2015). *Benefits and Challenges of Implementing Carbon Capture and Sequestration Technology in Nigeria*. 42–49.

Zhou, Q., Birkholzer, J. T., Tsang, C.-F., & Rutqvist, J. (2008). A method for quick assessment of CO2 storage capacity in closed and semi-closed saline formations. *International Journal of Greenhouse Gas Control, 2*(4), 626–639.